Investigation of anion transport in layered titanium carbide electrides

By
Duc Le

Senior Honors Thesis
Department of Chemistry
University of North Carolina at Chapel Hill

March 30th, 2026

Approved:

Professor Scott C. Warren, Thesis Advisor

Professor Yosuke Kanai, Reader

Professor Lina Quan, Reader

Abstract
Electrides are materials with anionic electrons located in lattice sites. This property makes them promising candidates for applications in catalysis and energy storage. Layered 2D electrides are a special class of electrides that feature electron gases confined in the interlayer space, and have received attention as candidate battery materials. It had been demonstrated that the 2D electride Y_2C is promising for application as an electrode in fluoride-ion batteries, which sparked our interest in isostructural materials like layered Ti_2C. However, anion intercalation in Ti_2C and other layered titanium carbides is poorly understood, and fluoride intercalation has not been previously investigated. In this study, we employ a combination of molecular dynamics, cluster expansion and Monte Carlo simulation, and DFT calculations to analyze the intercalation and diffusion properties of F^- inside layered Ti_2C electride and investigate its potential as a fluoride-ion battery electrode material. In addition, by comparing Ti_2C to isostructural materials like Y_2C and by analyzing diffusion of both H^- and F^-, we derived new guidelines for the development of 2D electrides as novel anion transport materials.

Introduction
Environmental impacts of fossil fuels have led to increased efforts in renewable energy research, with Li-ion batteries (LIBs) playing a central role. However, LIBs have drawbacks when put into use, such as flammability and supply chain issues[1]. Therefore, although studies on improving the safety and efficiency of LIBs remain an important and widely discussed topic, the interest on replacing Li^+ with other ion chemistries had also gained traction in the last decade. While most of the alternative solutions focus on replacing Li^+ with other more abundant cations like Na^+ [2] and Mg^{2+} [3], some researchers had explored F^- and have even demonstrated fluoride-ion batteries that can cycle reversibly[4] [5] [6](FIBs). Although research on FIBs is at an early stage, there are suggestions that FIBs can achieve high energy densities, large stability window, higher voltages, and higher Earth abundance of the raw components[4]. However, there remain significant challenges in discovering electrode and electrolyte materials that turn these theoretical predictions into experimental realities[5].

One of the most promising candidates for FIB electrodes is a class of solid materials named electrides. Electrides are interesting ionic solids that contain electrons located and localized in the lattice's anonic sites and act as normal anions[7] [8]. Because of this, electride materials typically have high electrical conductivities and low work functions, which made them attractive candidates for applications in electronics[8] [9], catalysis[8] [9], and battery electrodes[8] [9]. While the first mayenite-derived electrides (e.g. $[Ca_{24}Al_{28}O_{64}]^{4+}[4e^-]$) only had electrons in isolated cages[10], later computational and experimental studies had identified electride materials with electron sites linked into a higher-dimensional network[11], such as 1D (for example, Ca_3Si[12], Sr_3CrN_3[13]), 2D (Y_2C[14], Ca_2N[15]), and 3D (LaH_2[16]). This has led to studies exploring those electron frameworks as potential ionic diffusion pathways, which explains the interest in these materials as battery electrode candidates[8] [9]. In particular, layered 2D electrides, a special class of electrides that feature electron gases confined in the 2D interlayer spaces[17], had been studied as intercalation electrode materials[17] [18] [19]. Previous studies in our lab had proposed the concept of electrochemical electron-anion exchange, where the anionic electrons inside Y_2C are electrochemically exchanged with F^- without leading to redox reactions for the host material[20]. Other studies also identified that the 2D electride Y_2C is a promising candidate for fluoride-ion batteries[21]. However, yttrium, being a rare-earth metal, would pose significant barriers in the potential commercial adoption of FIBs if Y_2C is used

as an electrode material. Therefore, it is of importance that other materials with cheaper and more evenly distributed metals should be discovered for the commericalization of FIBs.

Reports on layered 2D Ti_2C have been made in literature[22 23 24]. The material is comprised of stacking Ti_2C monolayers, which belong to the widely studied class of MXene materials. Those materials have gained attention over the last decade as potential battery electrode materials, of which numerous studies and reviews had been published[25 26 27 28]. Compared to Y_2C, Ti_2C as a layered material is isostructural and features similar 2D electride nature and stacking sequence change behavior upon anion insertion[22 23 29], and it uses Ti as the metal element, which is much cheaper and more abundant than Y. However, while indeed there's been numerous studies on Ti_2C's potential as electrode materials, most of them only studied Ti_2C as a electrode material for LIBs and other cation batteries, and as the MXene monolayers instead of the layered electrides[26 27 28]. Studies on the anion intercalation into layered Ti_2C for the application in ion shuttling batteries as well as its electride properties are few and far in between. Luo et al. demonstrated that the hydrogenated Ti_2CH_2 is a promising cathode material for FIBs[30], however, as shown later in this study, hydrogenation of Ti_2C to Ti_2CH_2 would cause the material to lose its electride character, so the fluoride uptake properties of *electride* Ti_2C remains unknown. Therefore, we aim to investigate how F^- intercalates into layered Ti_2C, its diffusion properties inside the material, as well as how the stacking sequence change of Ti_2C changes upon fluoride intercalation / deintercalation, in order to determine its usefulness as a potential FIB electrode material.

Regarding hydrogenation of Ti_2C, another important application of electrides are in hydrogen storage materials. Hosono et al. reported various hydride-based electride materials based on rare earth hydrides LnH_2 (Ln = La, Y, Ce) that can be used as hydrogen storage materials[16]. In addition, even monolayer Ti_2C[31] had been investigated as potential hydrogen storage materials. It had been proved that in these cases, the hydrogen atom exists as negatively charged H^- inside the electride materials[31]. However, like in the case of F^-, the intercalation properties of H^- into layered Ti_2C have not been studied. The H^- ion, having the same charge, somewhat comparable size, yet distinctly difference in polarizability to F^-, offers an useful comparison case. Therefore, another goal in this study is to investigate the intercalation, diffusion, and phase equilibrium behaviors of H^- into Ti_2C and compare them to F^-, which help us to obtain new helpful insights into how negatively charged ions behave in these electride materials.

In this study, we performed computational studies to investigate the intercalation and diffusion properties of H^- and F^- inside Ti_2C. The energetics of anionic intercalation into Ti_2C, as well as the structural and electronic properties of layered Ti_2C electride before and after anion intercalation were studied using density functional theory (DFT) and charge analysis. The cluster expansion (CE) and Monte Carlo simulation methods were employed in studying the arrangement of the anions inside layered Ti_2C and the equilibrium phase behavior during intercalation and deintercalation. Finally, the diffusion properties of H^- and F^- inside layered Ti_2C were investigated by molecular dynamics (MD) and nudged elastic band (NEB) calculations. From these calculations, we are able to assess important performance characteristics of layered Ti_2C as a FIB electrode material. In addition, by studying the differences in the behavior of H^- and F^- inside 2D electrides, and the differences in material properties between Ti_2C and Y_2C as described in the previous paragraph, we develop improved understanding about how anions move in electrides. In addition, investigating the hydride uptake behavior of Ti_2C provides useful guidance on the experimental synthesis of the material, since the hydrogenated Ti_2CH_2 can be a precursor to the synthesis of Ti_2C electride.

Results and Discussion

I. Fluoride intercalation into Ti_2C

1. Thermodynamics and phase behavior of the Ti_2C-F system

It has been shown in previous studies that layered Y_2C exists in two stacking sequences: the O3 phase with ABC stacking sequence and space group $R\bar{3}m$ (Fig 1a), and the T1 phase with AA stacking sequence and space group $P\bar{3}m1$ (Fig 1b), in which the O3 is thermodynamically more stable before fluorination, but the T1 phase is more stable upon intercalation of more than 1 F per formula unit[20]. Since Ti_2C is isostructural to Y_2C, I hypothesized that this phase behavior might also appear in the Ti_2C-F system. Therefore, the energies of the two phases of Ti_2C before and after fluorination were calculated using DFT, and the results are shown in Fig 1c.

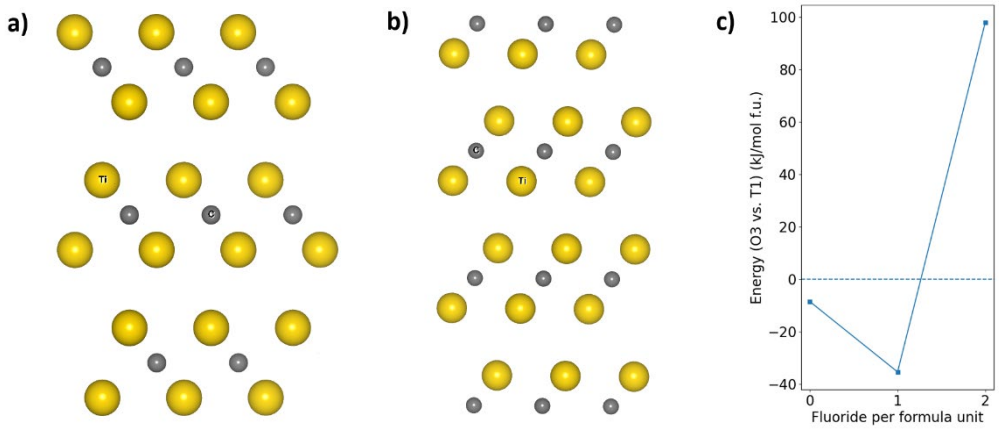


Figure 1: a) The structure of O3 Ti_2C; b) The structure of T1 Ti_2C; c) Relative stabilities of the O3 and T1 phases at 0K as calculated by DFT. Points below the dotted line suggests that the O3 phase is more stable, while those above the dotted line suggests that the T1 phase is more stable.

It can be seen from Fig 1c that the phase behavior of the Ti_2C-F system at 0K follows the same pattern as the Y_2C-F system as expected. The O3 phase is 8.61 kJ/mol more stable than the T1 phase before fluorination. However, after insertion of 2 fluoride ions per formula unit (giving an empirical formula of Ti_2CF_2), the T1 phase is 97.9 kJ/mol more stable. This change in phase stability is explained by the fact that insertion of more than 1 fluoride per formula unit requires the occupation of tetrahedral sites in the lattice. For the T1 structure, the tetrahedral sites are in a staggered conformation with respect to the nearby carbide ions (Fig 2a), which greatly reduces F-C anion-anion repulsions compared to the eclipsed conformation in the O3 structure (Fig 2b).

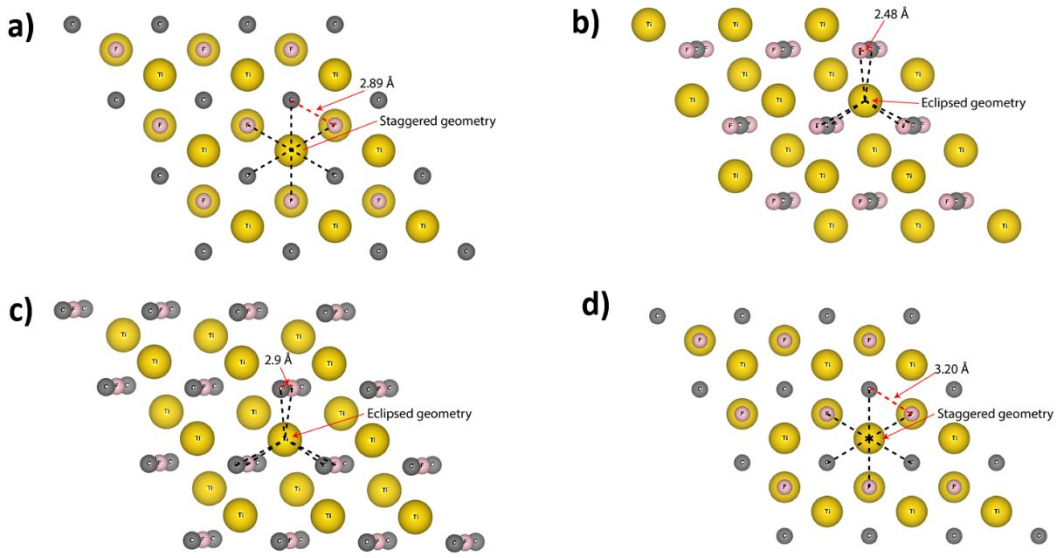


Figure 2: a): T1 phase Ti_2CF_2, showcasing longer C-F distances (2.89 Å); b): O3 phase Ti_2CF_2, showcasing shorter C-F distances (2.48 Å); c) T1 phase Ti_2CF, showcasing shorter C-F distances (2.9 Å); d) O3 phase Ti_2CF, showcasing longer C-F distances (3.20 Å) and a C-Ti-F twist angle of 60°

Putting 1 fluoride per formula unit in either O3 or T1 phases results in the complete occupation of the octahedral sites. From Fig 1c, the O3 Ti_2CF is 35.4 kJ/mol more stable than the T1 Ti_2CF at 0K. This reversal of stability compared to Ti_2CF_2 can be attributed to the same reason as above. In T1 Ti_2CF, the titanium atom has a distorted trigonal prismatic geometry (Fig 2c), which results in larger electrostatic repulsion between the fluoride and carbide ions, compared to the distorted octahedral geometry in the O3 Ti_2CF (Fig 2d). Regardless, the O3 Ti_2CF is actually found to be unstable, decomposing to O3 Ti_2C and T1 Ti_2CF_2 with a reaction enthalpy of -14.5 kJ/mol. Indeed, this instability of the intermediate O3 M_2CF is also found in the Y_2C-F system[20].

Simple DFT calculations are not enough to explore the phase space of the Ti_2C-F system in detail. Firstly, the Born-Oppenheimer approximation in DFT means that the results of these calculations are only valid at 0 K[32]. Secondly, the intermediate concentrations of F inside Ti_2C allow for a large number of possible arrangements of F in the material, and carrying out DFT calculations for all of these possible structures is impractical. To solve this problem, I use the cluster expansion method combined with Monte Carlo simulations. A cluster expansion model uses DFT data from a subset of training structures to extract the F-F and F-vacancy interactions (henceforth denoted as "effective cluster interactions" or "ECI")[33 34]. By approximating the structure's energy as a linear combination of these ECIs and the "background energy" (in this case, the Ti_2C lattice, which are assumed to be unchanged), the energy of any arrangement of F inside Ti_2C can be easily calculated. This allows one to carry out a Monte Carlo simulation in the semi-grand canonical ensemble[34 35], which gives a graph relating the chemical potential of fluoride to the fluoride concentration inside Ti_2C. This can be integrated to give the free energy of the phase as a function of F concentration at a non-zero temperature, enabling the construction of a phase diagram of the system.

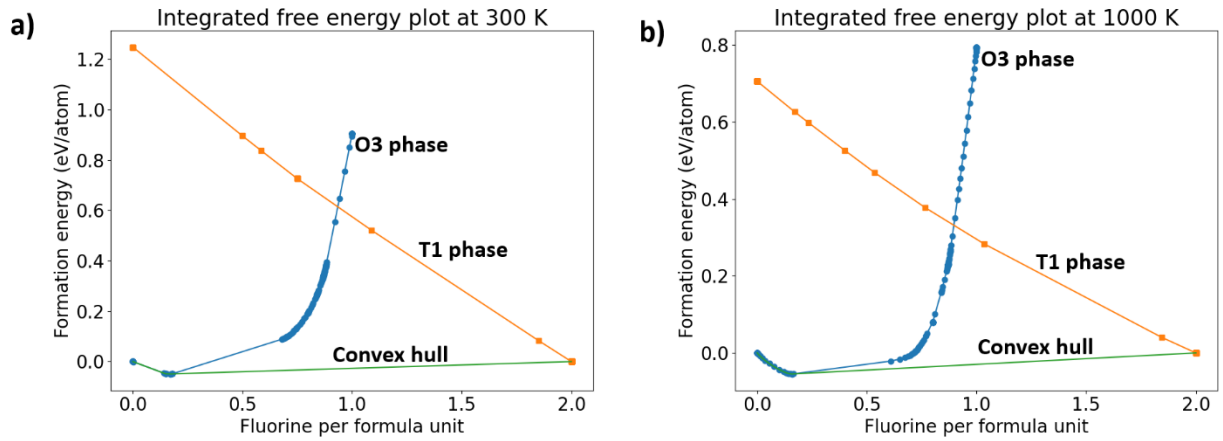


Figure 3: Integrated free energy curves for the two Ti_2C phases at 300 K (a) and 1000 K (b) as a function of number of F ions per formula unit, obtained from semi-grand canonical Monte Carlo simulations. The formation energies are calculated with respect to the O3 Ti_2C and T1 Ti_2CF_2

Figure 3 shows the integrated free energy curves for the two Ti_2C phases at 300 K and 1000 K as a function of number of fluoride per formula unit. It can be seen that at zero F concentration, the O3 phase is more stable than the T1 phase, up to at least 1000 K; on the other hand, at complete fluorination, the T1 phase is more stable. Interestingly, except for the Ti_2CF_2 point, the energy curve for the T1 all lies above the 0 eV/atom mark, suggesting that all intermediate configurations for the T1 Ti_2CF_x are unstable. This behavior is also seen in the Y_2C-F system[20]. For the O3 phase, the free energy curve at 300 K reveals that there is an isolated area of stable configurations (with negative formation energy and lie on the convex hull) in the range of $Ti_2CF_{0.14}$ to $Ti_2CF_{0.18}$. However, at 1000 K, this area merges with the Y_2C phase region to turn into a smoothly single-phase region from the unfluorinated Ti_2C to $Ti_2CF_{0.16}$, which is now similar to the behavior of the Y_2C-F system, though the limit of fluorination is slightly lower, being $Ti_2CF_{0.16}$ compared to $Y_2CF_{0.25}$. This may be explained by the fact that Ti_2C has a smaller volume and therefore can accommodate less F than Y_2C. Beyond these single-phase areas of the O3 phase however, is a single two-phase region where the O3 Ti_2CF_x ($x \sim 0.16$-0.18) and T1 Ti_2CF_2 coexists, which once again resemble the Y_2C-F system. The full calculated phase diagram is shown in Figure 4 below.

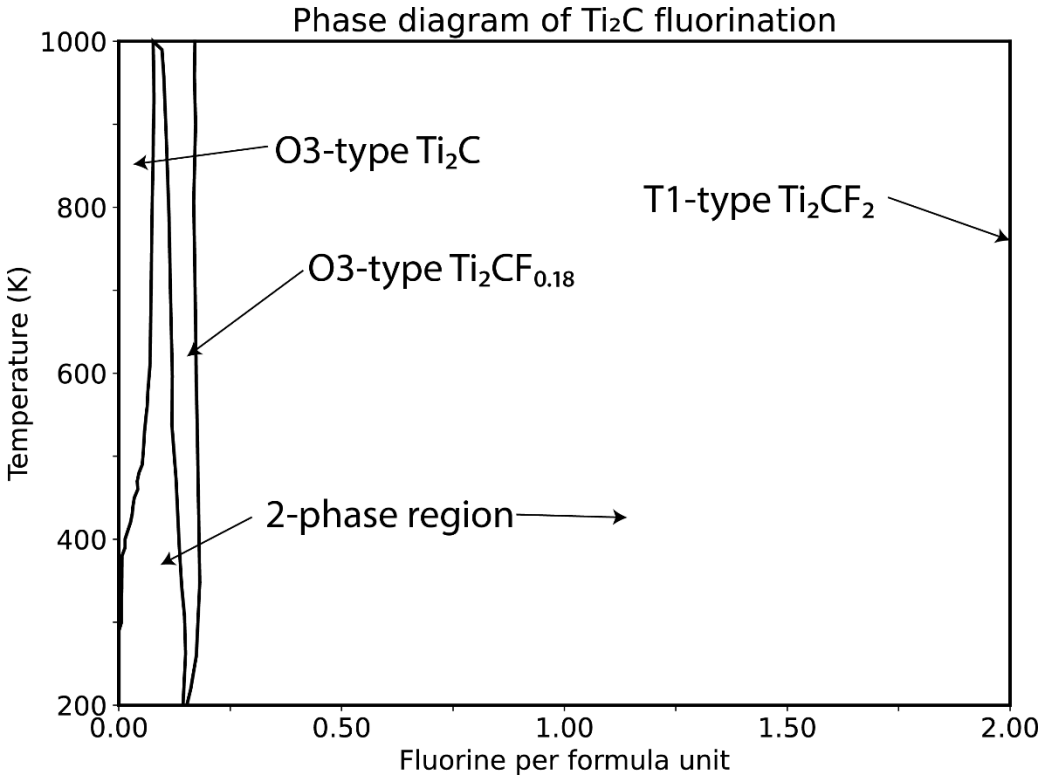


Figure 4: Calculated phase diagram of the Ti_2C-F system

Another feature of interest in these energy curves are the existence of several metastable configurations around $Ti_2CF_{0.75}$, especially in the free energy curve at 1000 K, where their formation energies become negative. However, soon after the $Ti_2CF_{0.75}$ mark, the formation energies for the O3 phase increase rapidly. To take a look into the potential metastable structure, I carried out a Monte Carlo annealing in the grand canonical ensemble (with fixed F concentration), and obtained an ordered structure with space group C2/m as seen in Fig 5a. We see that this structure features an ordered arrangement of three different 1D fluoride-vacancy chains that are parallel to the x or y axes (Fig 4b): the first chain fully occupied by F^-, the second chain has a vacancy after every three fluoride ions, and the third one has two vacancies after every two fluoride ions. I hypothesize that this arrangement serves to minimize electrostatic repulsions between the fluoride ions. Insertion of another fluoride ion into one of these vacancies will lead to massive electrostatic repulsions with the four neighboring fluoride ions and cause a great increase in energy.

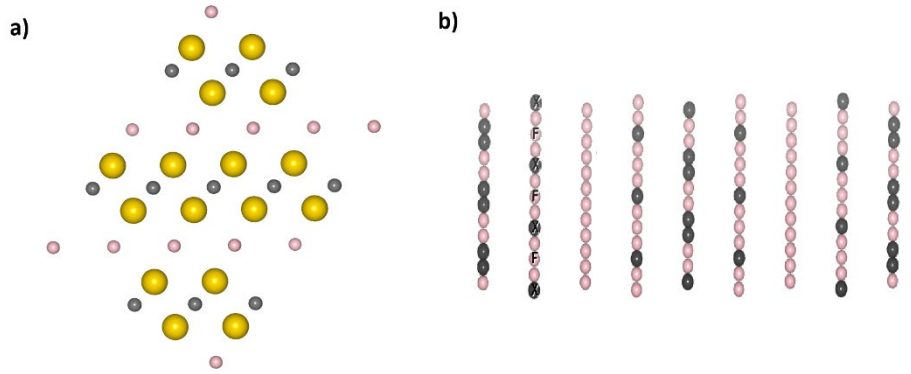


Figure 5: a) A primtive unit cell of the $Ti_2CF_{0.75}$ structure obtained from grand canonical annealing. The initial structure was equilibriated at a high temperature (1000 K) before being cooled down to 300 K. The conventional standard unit cell is highlighted by the box. Atom colors: Ti: light blue; C: brown; F: gray. b) The arrangement of fluorides and vacancies (denoted as X) in one interlayer space.

With the stable phases of Ti_2C before and after fluorination being identified, an estimation of the potential of electron insertion into Ti_2CF_2 can be made. Using the same approximation process by Druffel et al.[20], the potential of electron insertion into Ti_2CF_2 is calculated to be 1.60 V vs. Li/Li^+, which is about the same as lithium titanate oxide (LTO) anodes[36] (1.55 V vs. Li/Li^+). In addition, the maximum gravimetric capacity of Ti_2CF_2 is calculated to be 497.6 mAh/g, which is in-between Y_2CF_2 (282 mAh/g) and Sc_2CF_2 (526 mAh/g), which is expected since Ti is significantly lighter than Y and slightly heavier than Sc. Ti_2CF_2 also offers a good volumetric capacity at 1706 mAh/cm^3, which is even slightly higher than Sc_2CF_2 at 1634 mAh/cm^3.

2. Kinetics of fluoride diffusion in Ti_2C

With the established thermodynamic properties of Ti_2C as a fluoride-ion battery electrode as described above, the next step is to explore the kinetics of the fluoride diffusion inside Ti_2C. For each of two Ti_2C phases, I used the flare[37 38 39 40] code to construct a machine-learned force field for the movement of F inside the Ti_2C lattice. The obtained force field was then used to run LAMMPS[41 42]molecular dynamics simulations of the system at different temperatures. For the T1 Ti_2C phase, a supercell with the formula $Ti_{512}C_{256}F_{496}$ ($Ti_2CF_{1.93}$, corresponding to 256 primitive cells) was used in the MD simulation. For the O3 Ti_2C phase, a supercell with the formula $Ti_{432}C_{216}F_{54}$ ($Ti_2CF_{0.25,}$ corresponding to 72 primitive cells) was used. Even though the fluoride concentrations of these supercells lie slightly outside the single-phase regions in the system's phase diagram above, they're observed to be sufficiently metastable at the simulation temperature range and time scale.

MD simulations of each phase were carried out using a NVT ensemble at a temperature range of 1100 – 1700 K (for T1 phase) and 1200 – 1700 K (for O3 phase), with 100 K intervals and a 1 fs timestep. The simulations were run for 11 days in real time, yielding a simulation time between 2 - 4 ns (depending on the computing node used). From the MD trajectory, the mean-squared displacement of the F ions (and subsequently, the diffusion coefficients and diffusion barrier) can be obtained. The Arrhenius plots of the O3 and T1 phases are shown in Fig 6.

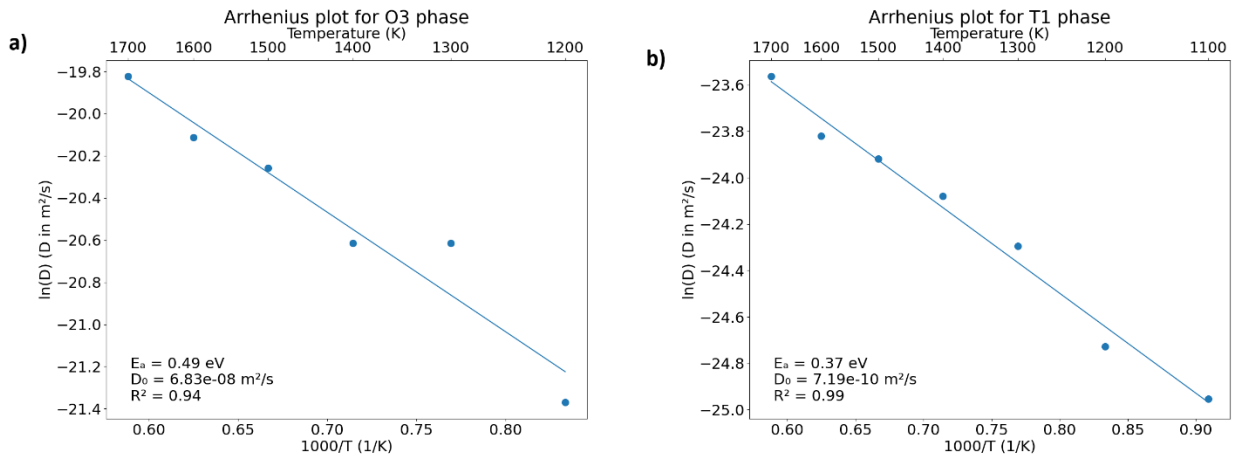


Figure 6: Arrhenius plots for calculation of the fluoride diffusion barrier in O3 phase Ti_2C (a) and T1 phase Ti_2C (b). For the O3 phase, the obtained diffusion barrier is 0.489 eV with a R^2 value of 0.937. For the T1 phase, the obtained diffusion barrier is 0.371 eV with a R^2 value of 0.986.

From the Arrhenius plots, the diffusion barrier of F inside Ti_2C is 0.371 eV and 0.489 eV for the T1 phase and O3 phases, respectively. Extrapolation of the least-square fitted line to T = 300 K gives the diffusion coefficient of F diffusion inside Ti_2C to be $4.19 * 10^{-12}\ cm^2\ s^{-1}$ for the T1 phase and $4.24 * 10^{-12}\ cm^2\ s^{-1}$ for the O3 phase.

In addition to MD simulation, the diffusion barrier of F inside T1 Ti_2C was also studied using the nudged elastic band (NEB) method. For this calculation, a supercell with the formula $Ti_{64}C_{32}F_{63}$ ($Ti_2CF_{1.97}$, corresponding to 32 primitive cells) was used. Due to the occupation of octahedral sites by F^- in the T1 phase being unfavorable (as described above), I hypothesized that the direct hopping of F^- between tetrahedral sites is the predominant pathway, instead of a two-step process where the F^- stays in the octahedral sites as an intermediate. This is further supported by Fig 7a, where it can be seen that the fluoride ions predominantly stay in the tetrahedral sites. Therefore, this pathway was used for the NEB calculation. The calculation yielded a diffusion barrier of 0.26 eV, which is slightly slower than the value obtained from MD. This is likely due to the fact that the NEB calculation is, by definition, performed at 0K and therefore only consisted of potential energy contributions, whereas the MD simulations were performed at finite temperatures and implicitly included entropic contributions.

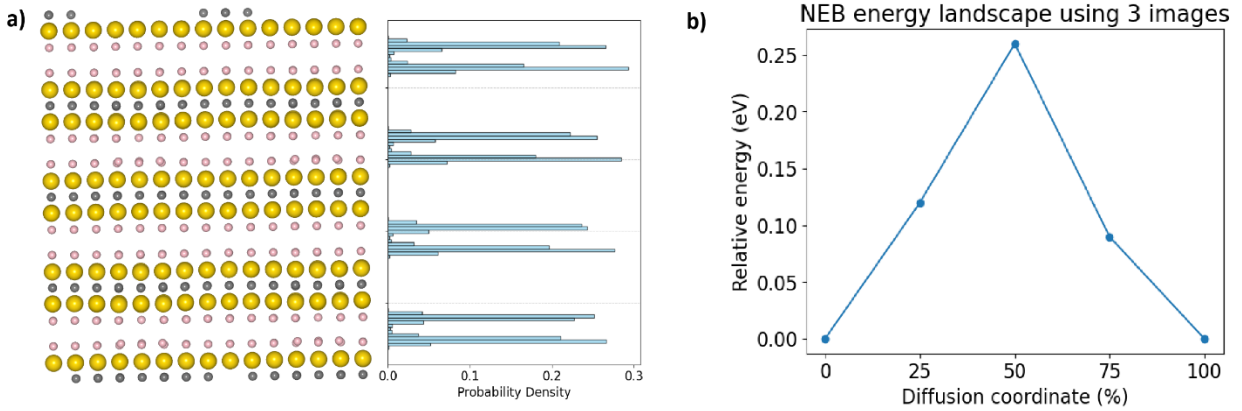


Figure 7: a) Probability density histogram of the z-coordinate of the fluoride ions during MD simulation, put next to the T1 phase simulation super cell using the same z-axis. The fluoride ions predominantly reside in the tetrahedral sites, suggesting that the

mechanism of F diffusion is the direct hopping between tetrahedral sites. b) Energy landscape of the diffusion process calculated from NEB using the direct hopping pathway and 3 intermediate images. The obtained diffusion barrier is 0.26 eV.

3. Structural and electronic properties of electride and fluoride inside Ti_2C

The NEB calculation above also provides a gateway to investigate the redox changes inside Ti_2C during the fluoride diffusion process. Previously, the concept of electrochemical electron–anion exchange (EAX) was demonstrated computationally in Y_2C, where the insertion and diffusion of F inside Y_2C causes no redox changes to the lattice[20]. Therefore, I was interested to investigate whether this concept would also apply to Ti_2C. Using the Badelf[43] code to analyze the charge density and electron localization function (ELF) data, I can compute the oxidation state and the volume of the atoms inside the ground state and transition state of the diffusion process, as well as the original Ti_2C and the fluorinated Ti_2CF_2 structures. The results are summarized in Table 1, and visualized in Figures 8a and 8b.

Structure	Ti		C		F		e^- charge
	Ox. state	Volume (Å^3)	Ox. state	Volume (Å^3)	Ox. state	Volume (Å^3)	
Ti_2C	+2.50	5.28	-2.75	14.75	N/A	N/A	-0.64 (tetrahedral) -0.95 (octahedral)
Ti_2CF_2	+2.45	5.61	-3.23	17.24	-0.83	11.85	N/A
$Ti_2CF_{1.97}$ (gs)	+2.46	5.62	-3.25	17.32	-0.84	12.23	-0.95
$Ti_2CF_{1.97}$ (ts)	+2.46	5.60	-3.27	17.53	-0.84	12.75	-0.16

Table 1: Charge and volume analysis of atoms and electride sites in T1 phase Ti_2C. For the ground state and transition state structures, the values reported for Ti and C are the global average, while the values for F are for the diffusing ion. A detailed description of the changes to Ti and C atoms proximal to the diffusion process is visualized in Figures 7a and 7b

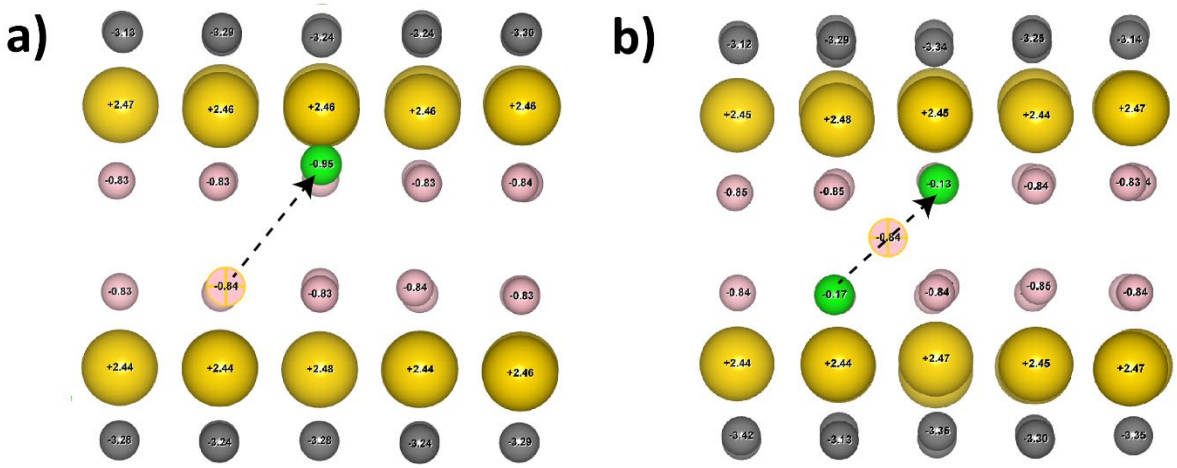


Figure 8: Atom labels: Ti: gold, C: grey, F: pink, electron: green. a) Oxidation states of proximal atoms to the F^- diffusion process in the ground state. b) Oxidation states of proximal atoms to the F^- diffusion process in the transition state. The moving fluoride ion is highlighted, and the path is denoted by an arrow.

From the results, we see that T1 Ti_2C is an electride with three distinct electride sites per formula unit: two at the tetrahedral sites and one at the octahedral site. The Ti and C atoms are assigned an oxidation state of approximately +2.5 and -2.75 respectively. The octahedral electride site is

assigned a charge of -0.95, while each tetrahedral electride site has a charge of -0.64, integrating to 2.24 electrides per formula unit. Upon complete fluorination, the Ti atom's oxidation state remains practically unchanged at +2.45, however, the C atom is reduced to an oxidation state of -3.23, accompanied by a increase in volume from 14.8 $Å^3$ to 17.2 $Å^3$. The two F ions have an oxidation state of -0.83 each and a volume of 11.85 $Å^3$. This means that adding two fluoride ions into Ti_2C is not enough to completely replace the electrides' negative charge, forcing the carbon to take in the excess negative charge and be reduced. This is in contrast to Y_2C, where similar analyses reveal that the Y and C atoms' oxidation states are +2.34 and -2.99 respectively before fluorination, and +2.41 and -3.07 respectively after fluorination (i.e. minimal changes), while the two fluoride ions (oxidation state -0.87) almost completely exchange for the two electride electrons (charge -0.84; 1.69 electrides per formula unit). This means that the concept of electrochemical anion exchange only applies partially to T1 Ti_2C, as the carbon atoms are significantly reduced during fluorination. Building up negative charges on C is unfavorable, which may partially explain the instability of intermediate T1 Ti_2CF_x structures as observed during the cluster expansion and Monte Carlo process above.

Another important factor of EAX and a good electrode material is the small change in the host lattice's volume after fluorination[20]. Unfortunately, this is not true for Ti_2C. For the T1 phase, full structural relaxation of Ti_2CF_2 leads to the interlayer distance increasing from 2.59 Å to 4.11 Å, an increase of 58.61%. This corresponds to an increase from 4.92 Å to 6.33 Å (28%) in the **c** lattice constant of the unit cell. While the **a** lattice constant of Ti_2C does not increase appreciably (from 3.06 Å to 3.08 Å), the large increase in the **c** lattice constant was sufficient to cause a large increase in volume of the unit cell upon fluorination (39.93 $Å^3$ to 52.16 $Å^3$, a 30% change).

Next, I investigated the changes of the Ti_2C lattice during the diffusion process. Removing one fluoride from the fully fluorinated supercell creates an electride site with 0.95 electrons (where a fluoride would eventually migrate to), but does not significantly change the oxidation state or volume of the nearby atoms, besides some very slight reductions of nearby Ti and C atoms, but in any case, the changes in oxidation state remains mostly less than 0.05 (Fig. 8a). The fluoride that would migrate has its volume slightly increased to 12.23 $Å^3$ and its oxidation state slightly decreased to -0.84. In the transition state, the moving fluoride occupies the midpoint between the two tetrahedral sites that had low ELF values in the original Ti_2C electride. Its volume increases to 12.74 $Å^3$, which is presumably expected due to it now being in a site with octahedral geometry, though its oxidation state remains at -0.84. The anionic electron now simultaneously occupies both the initial and final site, though it now only has 0.30 electrons, likely because of slight partial reduction of nearby carbons (Fig 8b). As seen in Fig. 8a and 8b, the oxidation states of the nearby atoms during the diffusion process does not change significantly, except the carbons that are slightly reduced as described above. From these, we can see that neither the fluoride ion nor the Ti_2C host lattice undergo any significant redox changes during the diffusion process.

In sort, from these calculations, I had established that while layered Ti_2C electride is a potential candidate for FIB battery electrodes, with a good theoretical capacity, diffusion barrier, and redox potential, it suffers from a few disadvantages compared to Y_2C, namely the significant changes in the Ti_2C host lattice upon fluorination, which involves reduction of carbon ions and large expansion in volume.

II. Hydride intercalation into Ti_2C

1. Thermodynamics and phase behavior of the Ti_2C-H system

In addition to batteries, hydrogen storage materials is also an important topic of research in the field of clean and renewable energy. Since 2D MXenes of the formula M_2C, which includes Ti_2C, had been studied as potential hydrogen storage materials[44], I'm also interested in studying the potential of layered Ti_2C as a potential hydrogen storage material. In addition, the hydride ion has both significant similarities and differences from fluoride, and this means that understanding the similarities and differences of their behaviors inside a material can help uncover insights in how anions behave inside electride materials and help devise new guidance on designing anion-conducting materials.

First, I was interested to see whether the phase behavior of the Ti_2C-H system would follow the Ti_2C-F system as described in the previous section. The energies of the two phases of Ti_2C before and after hydrogenation were calculated using DFT, and the results are shown in Fig 9.

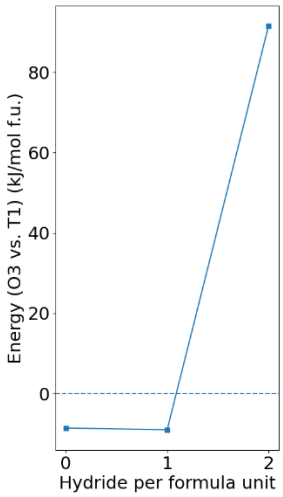


Figure 9: Relative stabilities of the O3 and T1 phases at 0K as calculated by DFT. Points below the dotted line suggests that the O3 phase is more stable, while those above the dotted line suggests that the T1 phase is more stable.

It can be seen from Fig 8 that the phase behavior of the Ti_2C-H system at 0K follows the same pattern as the Ti_2C-F system as expected. After insertion of 2 hydride ions per formula unit (giving an empirical formula of Ti_2CH_2), the T1 phase is 91.6 kJ/mol more stable. Putting 1 hydride per formula unit in either O3 or T1 phases result in the complete occupation of the octahedral sites, in which the O3 Ti_2CH is 9.02 kJ/mol more stable than the T1 Ti_2CH at 0K. The O3 Ti_2CH is also unstable, decomposing to O3 Ti_2C and T1 Ti_2CH_2 with a reaction enthalpy of –12.78 kJ/mol. Therefore, the phase behavior at 0K of the Ti_2C-H system is similar to the fluoride counterpart, though the magnitudes of stability/instability seem to be smaller. This can be explained by the fact that since most of the instabilities come from anion-anion repulsions, a smaller hydride (which will be proven in the next sections) will cause less repulsion than a bigger fluoride.

Next, I use the same cluster expansion method combined with Monte Carlo simulations as above to investigate the phase behavior of the Ti_2C-H system at finite temperatures. The exact same procedure used for the determination of the phase behavior of the Ti_2C-F system in the previous section was used. Figure 10 shows the integrated free energy curves for the two Ti_2C phases at 300 K and 1000 K as a function of number of hydride ions per formula unit.

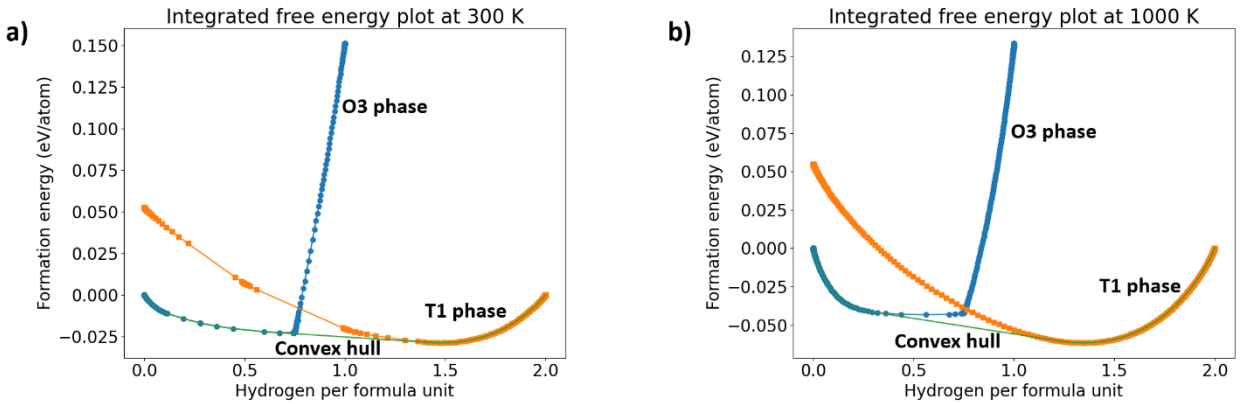


Figure 10: Integrated free energy curves for the two Ti_2C phases at 300 K (left) and 1000 K (right) as a function of number of H ions per formula unit, obtained from semi-grand canonical Monte Carlo simulations. The formation energies are calculated with respect to the O3 Ti_2C and T1 Ti_2CH_2

Compared to the free energy curves of the Ti_2C-F system, the free energy curves of the Ti_2C-H system features significant differences, mostly in the curve for the T1 phase. Unlike in the fluoride system, the energy curve of the T1 phase now features a continuous, negative formation energy, single-phase region that runs from Ti_2CH_2 to approximately $Ti_2CH_{1.30}$ (at 300 K) or $Ti_2CH_{1.22}$ (at 1000 K). This suggests that insertion of H^- into T1 phase Ti_2C is more thermodynamically favorable than insertion of F^-; a possible rationale of this will be proved in t`he next sections. On the other hand, the O3 phase's energy curves more resemble their fluorination counterparts, especially the free energy curve of the O3 phase's fluorination at 1000 K (see Fig 3b). This is evident in several features such as a continuous single phase region from Ti_2C to $Ti_2CH_{0.11}$ (for 300 K) or $Ti_2CH_{0.25}$ (for 1000 K), and the drastic increase in energy after the $Ti_2CH_{0.75}$ mark. However, the energy curves of the O3 phase's hydrogenation also features several difference stable arrangements between $Ti_2CH_{0.25}$ and $Ti_2CH_{0.75}$.

Since both the energy curves of the fluorination and hydrogenation of O3 phase Ti_2C feature similar jumps after the $Ti_2CH_{0.75}$, I performed a grand canonical annealing simulation to take a look at the ordered structure that theoretically forms in this concentration. Figure 11 shows the conventional unit cell of that structure, which unlike in the Ti_2C-F system, has space group C2 (Figure 11a).

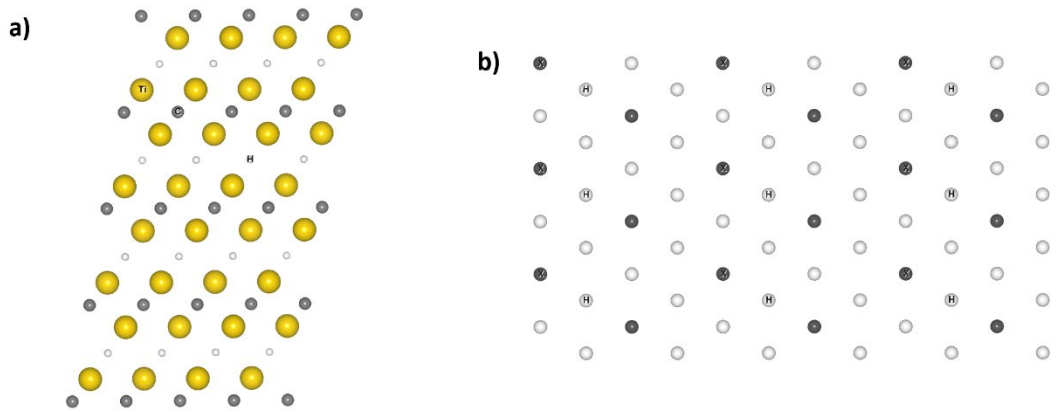


Figure 11: a) a primitive unit cell of the $Ti_2CH_{0.75}$ structure obtained from grand canonical annealing. The initial structure was equilibriated at a high temperature (1000 K) before being cooled down to 300 K. b) The arrangement of hydrides and vacancies (denoted as X) in one interlayer space.

Similar to the structure in Fig 4, this one also features chains of hydrides parallel to the x or y axes with patterns of vacancies (Fig 11b). However, this structure only features two types of hydride chains: one type with no vacancies and the other type has alternating hydrides and vacancies. I theorize that the reason behind the large jump in energy by inserting hydride into this structure also comes from increased anion-anion repulsions, and the different pattern of hydrides may arise from the differences in the anions' size and the structural changes they impose to the host lattice.

2. Kinetics of hydride diffusion in Ti_2C

Secondly, using similar methods as in the previous sections, I explored the kinetics of hydride diffusion inside Ti_2C. For each of two Ti_2C phases, I used the flare code to construct a machine-learned force field for the movement of H inside the Ti_2C lattice. The obtained force field was then used to run LAMMPS molecular dynamics simulations of the system at different temperatures. For the T1 Ti_2C phase, a supercell with the formula $Ti_{512}C_{256}H_{480}$ ($Ti_2CH_{1.875}$, corresponding to 256 primitive cells) was used in the MD simulation. For the O3 Ti_2C phase, a supercell with the formula $Ti_{432}C_{216}H_{54}$ ($Ti_2CH_{0.25,}$ corresponding to 72 primitive cells) was used. Unlike the fluorinated system, the hydride concentrations of these supercells lie inside the single-phase regions in the system's phase diagram above.

MD simulations of each phase were carried out using a NVT ensemble at a temperature range of 1100 – 1700 K (for T1 phase) and 1200 – 1700 K (for O3 phase), with 100 K intervals. Due to hydrogen's low mass, the timestep was reduced to 0.1 fs. The simulations were run for 11 days in real time, yielding a simulation time between 0.2 – 0.4 ns (depending on the computing node used). From the MD trajectory, the mean-squared displacement of the H ions (and subsequently, the diffusion coefficients and diffusion barrier) can be obtained. The Arrhenius plots of the O3 and T1 phases are shown in Fig 12.

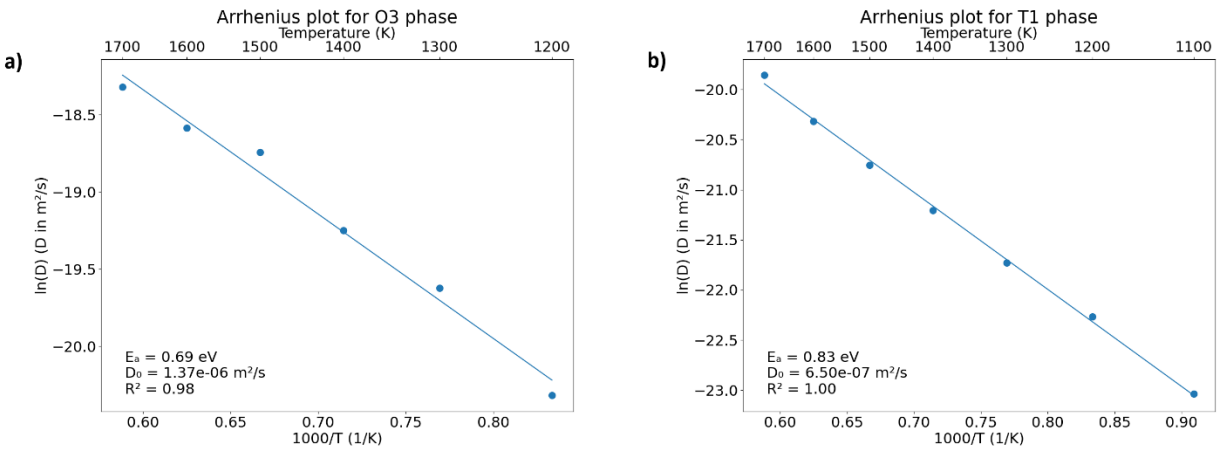


Figure 12: Arrhenius plots for calculation of the hydride diffusion barrier in O3 phase Ti_2C (left) and T1 phase Ti_2C (right). For the O3 phase, the obtained diffusion barrier is 0.694 eV with a R^2 value of 0.984. For the T1 phase, the obtained diffusion barrier is 0.835 eV with a R^2 value of 0.998.

From the Arrhenius plots, the diffusion barrier of H inside Ti_2C is 0.83 eV and 0.69 eV for the T1 phase and the O3 phase respectively. Notably, this is the opposite to the Ti_2C-F system, as in this case, the O3 phase has a lower diffusion barrier. However, regardless of phase, the diffusion barrier of hydride seems to be always higher than fluoride. Extrapolation of the least-square fitted line to T = 300 K gives the diffusion coefficient of H diffusion inside Ti_2C to be $4.98 * 10^{-17}\ cm^2\ s^{-1}$ for the T1 phase and $2.95 * 10^{-15}\ cm^2\ s^{-1}$ for the O3 phase.

The diffusion barrier of H inside T1 Ti_2C was also studied using the nudged elastic band (NEB) method like above. For this calculation, a supercell with the formula $Ti_{64}C_{32}H_{63}$ ($Ti_2CH_{1.97}$, corresponding to 32 primitive cells) was used. For comparison with the fluoride diffusion calculations, the same pathway with direct hopping between two tetrahedral sites was used for this NEB calculation. The calculation yielded a diffusion barrier of 0.71 eV, which is slightly slower than the value obtained from MD. Since a relatively similar difference in the diffusion barriers was also obtained in the Ti_2C-F system above, this further supports our hypothesis that these mismatch comes from the lack of entropic effects in NEB calculation, as because the MD calculations for the diffusion of F^- and H^- inside Ti_2C were carried out at similar temperatures and used similar structures, the value of $T\Delta S$ is likely to be similar across both calculations..

3. Structural and electronic properties of hydride inside Ti_2C

In order to investigate the difference in behavior between F^- and H^- inside Ti_2C, I once again used the Badelf code to analyze the changes in oxidation state and volume of the atoms inside the lattice during the hydride intercalation and diffusion processes. The results are summarized in Table 2 and Figure 13.

Structure	Ti		C		H		e^- charge
	Ox. state	Volume (Å^3)	Ox. state	Volume (Å^3)	Ox. state	Volume (Å^3)	
Ti_2C	+2.50	5.28	-2.75	14.75	N/A	N/A	-0.64 (tetrahedral) -0.95 (octahedral)

Ti_2CH_2	+2.46	5.22	-2.95	16.61	-0.98	7.30	N/A
$Ti_2CH_{1.97}$ (gs)	+2.48	5.15	-3.04	17.26	-0.96	7.01	-1.39
$Ti_2CH_{1.97}$ (ts)	+2.49	5.15	-3.05	17.27	-1.97	15.7	N/A

Table 2: Charge and volume analysis of atoms and electride sites in T1 phase Ti_2C. For the ground state and transition state structures, the values reported for Ti and C are the global average, while the values for H are for the diffusing ion. A detailed description of the changes to Ti and C atoms proximal to the diffusion process is visualized in Figures 12a and 12b

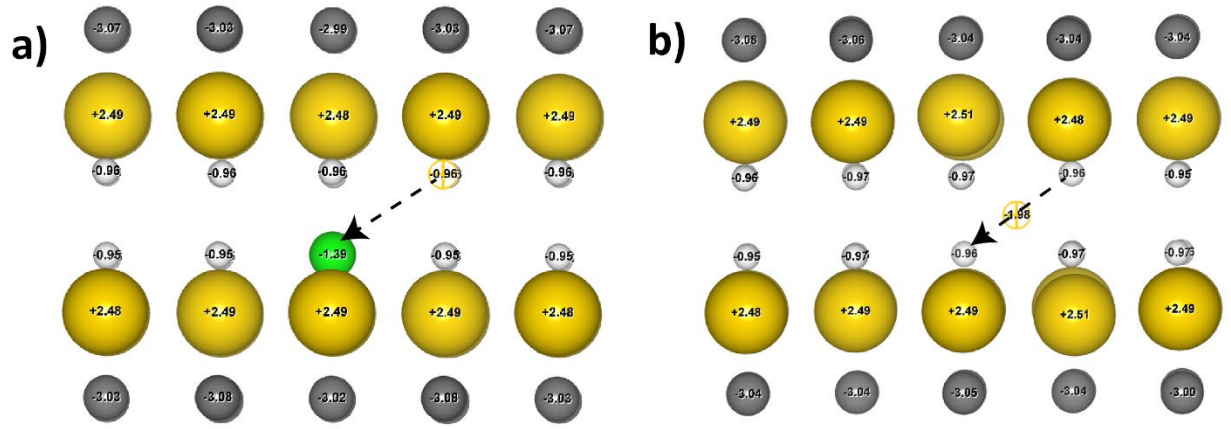


Figure 13: Atom labels: Ti: gold, C: grey, H: white, electron: green. a) Oxidation states of proximal atoms to the H^- diffusion process in the ground state. b) Oxidation states of proximal atoms to the H^- diffusion process in the transition state. The moving hydride ion is highlighted, and the path is denoted by an arrow.

From the results, upon complete hydrogenation, the Ti atom's oxidation state also remains practically unchanged at +2.46, the same as in Ti_2CF_2. The C atom is also reduced, though only to a smaller extent, from -2.75 to -2.95, accompanied by a smaller increase in volume from 14.8 $Å^3$ to 16.6 $Å^3$. Surprisingly, the two H^- ions have an oxidation state of -0.98 each (compared to -0.83 for F^-), and a volume of 7.3 $Å^3$, only about 60% the volume of F^- inside Ti_2CF_2. For comparison, similar calculations and analyses reveal that the oxidation state of H^- inside LiH is also -0.98, and that of H^- inside TiH_2 is -1.08. For the Ti_2C system, this is somewhat surprising since I originally hypothesized that F should have a more negative charge due to it being the more electronegative atom and forms the harder anion. Regardless, the higher negative charge provided by the two hydride ions into Ti_2C means that the carbons are less reduced, leading the system to behave more like the fluorination of Y_2C and electrochemical electron-anion exchange. For Y_2C, similar analyses reveal that the Y and C atoms' oxidation states are +2.34 and -2.99 respectively before hydrogenation, and +2.39 and -2.95 respectively after hydrogenation (i.e. minimal changes). Since the carbon atoms are now less reduced, this explains the higher favorability of hydrogenating Ti_2C than fluorinating Ti_2C. In addition, the smaller volume of hydride should also lead to a smaller volume expansion upon hydrogenation. Indeed, this is confirmed by the full structural relaxation of Ti_2CH_2, where it's found that the interlayer distance is only 2.69 Å, a mere 3.85% increase from the unhydrogenated material (2.59 Å).

Next, I investigated the changes of the Ti_2C lattice during the hydride diffusion process. Similar to the fluoride diffusion, removing one hydride from the fully hydrogenated supercell creates an electride site with 1.39 electrons (where a hydride would eventually migrate to), but does not significantly change the oxidation state or volume of the nearby atoms. The hydride that would migrate have its volume slightly decreased to 7 $Å^3$ and its oxidation state slightly increased to -0.96. In the transition state, the moving hydride also occupies the midpoint between the two

tetrahedral sites that had low ELF values in the original Ti_2C electride. However, in the transition state, remarkably, analysis of its volume gives a large value of 15.69 $Å^3$, and its oxidation state is found to be -1.98, which does not make chemical sense as this would entail adding an electron to the helium noble gas electron configuration. However, it's also noticed that the anionic electron from the ground state does not appear in the transition state as electride sites. A visualization of the electron localization function (ELF) (Fig 14a) shows that the ELF plot around the moving hydride seems to be elongated towards the two vacancy sites instead of being spherical, meaning that the H^- orbital may had some interactions or overlaps with the should-be electride orbitals. Therefore, the overal charge and volume obtained from Badelf is likely the combination of the hydride and the electride sites, which are treated as one by the code due to the interaction. A similar visualization of the ELF plot of the fluoride diffusion's transition state (Fig 14b) does not reveal this same interaction; the ELF plot around the moving fluoride are only very slightly elongated and there's a clear gap between the fluoride ELF basin and the electride ELF basins; notably, the ELF basins seem to be interacting with C atoms instead. This is likely due to the longer distance between the fluoride and the electride sites in the transition state (which is half the hopping distance, 2.1 Å for H and 2.5 Å for F), and the F^- ion being a hard ion and not easily polarized. In addition, a suggestion that the electride sites may favor interaction with soft ions like H^- and C^{2-} /C^{3-} over the hard F^- can also be made, though this requires further studies to be confirmed. Overall, this unique interaction of H^- with the electride sites seems to lead to the significantly higher observed diffusion barrier of H^- diffusion compared to F^- diffusion, as the interactions between the hydride and the electride sites are likely to be anion-anion repulsions in nature, which destabilizes the transition state. On the other hand, as seen in Fig 12a and 12b, the oxidation states of the nearby atoms during the diffusion process does not change significantly, similar to the fluoride diffusion.

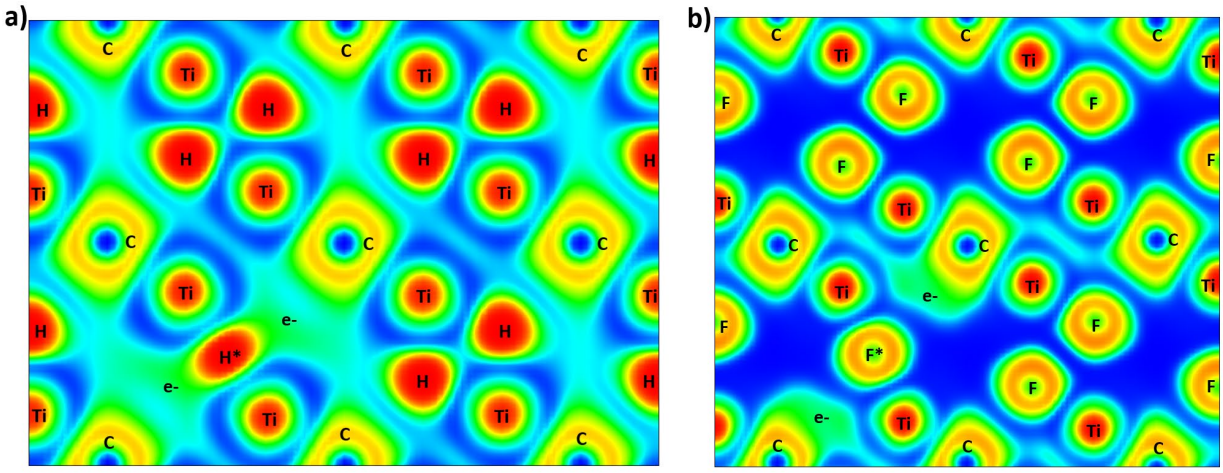


Figure 14: a) 2D ELF slice of the transition state of H^- diffusion inside Ti_2C, with atomic basins and electride basins labeled. The H atom denotes the moving hydride in its transition state, showing strong elongation towards the two electride sites. The ELF value at the two electride sites is 0.45. b) 2D ELF slice of the transition state of F^- diffusion inside Ti_2C, with atomic basins and electride basins labeled. The F* atom denotes the moving fluoride in its transition state, showing only slight elongation towards the two electride sites. The ELF value at the two electride sites is 0.30.*

In sort, these analyses show that while hydride can resemble fluoride in many aspects when interacting with layered electrides, there also exists stark differences between them, which primarily comes from the differences in size and polarizibility of the two ions.

III. Comparison of anion behavior in Ti_2C and other M_2C materials

1. Charge and volume of H^-, F^-, and electride electrons inside M_2C materials

In order to further probe the differences between H^- and F^- and how they behave inside different M_2C materials, in addition to calculations with Ti_2C and Y_2C already performed in the previous sections, I carried out DFT calculations and Badelf charge analyses on two other isostructural materials: Sc_2C[45] and Zr_2C[46]. Data of the oxidation state and volume of the metal ion, carbon, and H^-/F^-/electride electrons are presented in Table 3. Meanwhile, Table 4 describes the changes in the interlayer distance and **c** lattice constant upon hydrogenation or fluorination.

Table 3: Oxidation state and volume of atoms and electride sites inside different M_2C materials

Structure	M		C		F/H		e^- charge
	Ox. state	Volume (Å^3)	Ox. state	Volume (Å^3)	Ox. state	Volume (Å^3)	
Ti_2C (T1)	+2.50	5.28	-2.75	14.75	N/A	N/A	-0.64 (tetrahedral) -0.95 (octahedral)
Ti_2CF_2 (T1)	+2.45	5.61	-3.23	17.24	-0.83	11.85	N/A
Ti_2CH_2 (T1)	+2.46	5.22	-2.95	16.61	-0.98	7.30	N/A
Ti_2C (O3)	+2.36	6.04	-3.00	16.07	N/A	N/A	-1.71
Ti_2CF (O3)	+2.33	6.04	-3.74	20.64	-0.93	12.60	N/A
Ti_2CH (O3)	+2.44	5.30	-3.17	16.53	-1.12	8.88	N/A
Sc_2C (T1)	+2.22	6.86	-2.74	19.83	N/A	N/A	-0.86
Sc_2CF_2 (T1)	+2.26	6.91	-2.81	21.23	-0.86	13.03	N/A
Sc_2CH_2 (T1)	+2.23	6.73	-2.72	21.18	-0.87	9.77	N/A
Sc_2C (O3)	+2.23	6.92	-2.82	20.88	N/A	N/A	-1.63
Sc_2CF (O3)	+2.10	7.35	-3.24	23.95	-0.95	13.53	N/A
Sc_2CH (O3)	+2.17	6.83	-2.84	20.35	-0.97	11.06	N/A
Zr_2C (T1)	+2.81	7.84	-2.89	16.63	N/A	N/A	-0.73 (tetrahedral) -1.26 (octahedral)
Zr_2CF_2 (T1)	+2.72	8.58	-3.73	21.88	-0.85	12.21	N/A
Zr_2CH_2 (T1)	+2.78	7.75	-3.23	19.33	-0.99	7.71	N/A
Zr_2C (O3)	+2.17	8.19	-3.42	15.99	N/A	N/A	-0.92
Zr_2CF (O3)	+2.36	8.88	-3.13	19.38	-0.80	8.92	N/A
Zr_2CH (O3)	+2.37	8.62	-3.13	19.05	-1.23	10.18	N/A
Y_2C (T1)	+2.34	10.65	-2.99	24.07	N/A	N/A	-0.85
Y_2CF_2 (T1)	+2.41	10.30	-3.07	26.90	-0.88	12.98	N/A
Y_2CH_2 (T1)	+2.39	10.12	-2.95	26.03	-0.91	11.76	N/A
Y_2C (O3)	+2.36	10.48	-3.03	24.63	N/A	N/A	-1.69
Y_2CF (O3)	+2.22	11.07	-3.52	29.25	-0.93	13.27	N/A
Y_2CH (O3)	+2.29	10.44	-3.12	25.76	-1.04	13.83	N/A

Structure	Interlayer distance (Å)	c lattice constant (Å)

	Before intercalation	After intercalation	% change	Before intercalation	After intercalation	% change
Ti_2CF_2 (T1)	2.59	4.11	58.61%	4.92	6.33	28.78%
Ti_2CH_2 (T1)	2.59	2.69	3.85%	4.92	5.04	2.47%
Ti_2CF (O3)	2.54	3.23	26.74%	14.46	15.81	9.33%
Ti_2CH (O3)	2.54	2.57	1.15%	14.46	14.38	-0.57%
Sc_2CF_2 (T1)	3.19	3.83	20.19%	5.65	6.35	12.27%
Sc_2CH_2 (T1)	3.19	3.03	-5.04%	5.65	5.51	-2.52%
Sc_2CF (O3)	3.06	3.13	2.24%	16.58	16.41	-1.00%
Sc_2CH (O3)	3.06	2.83	-7.68%	16.58	15.67	-5.47%
Zr_2CF_2 (T1)	2.92	4.10	40.36%	5.46	6.52	19.57%
Zr_2CH_2 (T1)	2.92	2.93	0.47%	5.46	5.49	0.72%
Zr_2CF (O3)	1.55	1.68	8.36%	9.22	10.09	9.48%
Zr_2CH (O3)	1.55	1.66	6.72%	9.22	9.95	7.93%
Y_2CF_2 (T1)	3.52	3.61	2.51%	6.22	6.32	1.65%
Y_2CH_2 (T1)	3.52	3.30	-6.31%	6.22	6.00	-3.53%
Y_2CF (O3)	3.45	3.24	-6.20%	18.41	17.46	-5.12%
Y_2CH (O3)	3.45	2.63	-23.84%	18.41	17.19	-6.59%

*Table 4: Changes in the interlayer distance and **c** lattice constant upon hydrogenation or fluorination of different M_2C materials*

From the data, there are clear trends on the behavior of these material systems. For all M_2C materials, the oxidation states of the metal atoms are practically the same (around +2.5), both in the electride material and after anion intercalation. In the electride materials, the oxidation state of carbon is also more or less the same, being around -2.7 to -3.0. For M_2C materials featuring metals in Group 3 (Sc, Y), the carbon atoms are only very slightly reduced upon hydrogenation or fluorination. For M_2C materials with Group 4 metal (Ti, Zr), the carbons are more significantly reduced, and fluorination leads to a more significant reduction of the carbons. As established above, this is directly related to the properties of the anionic electride sites.

For Sc_2C and Y_2C in the T1 phase, each formula unit has 2 electride sites in tetrahedral sites, which integrates to less than 2 electride electrons per formula unit (1.69 for Y_2C and 1.71 for Sc_2C). These tetrahedral electride sites are connected by "bridges" of medium-high ELF value in the octahedral sites, creating a 2D network. On the other hand, for Ti_2C and Zr_2C, each formula unit has 3 electride sites: two in tetrahedral sites as described above, and one in the octahedral site, thus integrating to more than 2 electride electrons per formula unit (2.24 for Ti_2C and 2.73 for Zr_2C). The octahedral sites, instead of being "bridges" of medium-high ELF value in Sc_2C and Y_2C, now split into two different sites: an electride site with ELF value and a site with low ELF value. This is reminiscent of the Hf_2X-type (X = O, S, Se, Te) electrides, though in this case, the octahedral electride sites have the higher ELF maxima[47]. Since Ti_2C and Zr_2C has more than 2 electrides per formula unit, exchanging for two F^- or H^- per formula unit is not enough to completely replace the electride electrons' negative charge, and this mismatch would force the carbons to be partially reduced for charge balance.

For the O3 phase, the distinction between Group 3 and Group 4 metals are less clear and/or significant. All those materials have just one octahedral electride site per formula unit and no tetrahedral electride sites, and the electron count integrates to approximately 1.5-1.7 electrons per

formula unit, except for Zr_2C, which only has 0.92 electrons per formula unit. The trend of reduction of carbons upon hydrogenation/fluorination to compensate for the loss of negative charge (note that like in the T1 phase, we are exchanging one hydride/fluoride for more than one electron per formula unit). Once again, Zr_2C proves to be anomalously behaving, as structural relaxation of Zr_2CF and Zr_2CH even led to the loss of the 2D material character, so the O3 phase of Zr_2C would not be discussed for the rest of this section.

A final trend, as seen in Table 4, is that intercalation of fluoride into layered M_2C materials typically causes significant increases in interlayer distance, and by extension, volume. On the other hand, intercalation of hydride into layered M_2C materials usually leads to minimal changes in interlayer distance and volume. Notably, Sc_2CH_2 and Y_2CH_2 even slightly shrink upon hydrogenation. This can be explained by the larger volume of F^- compared to H^-. Since one of the most important criteria for a battery electrode or a hydrogen storage material is low volume change during insertion and de-insertion of ions, this provides an important point to consider in using these materials for battery or hydrogen storage applications.

2. Diffusion process of H^- and F^- inside M_2C materials

Next, the diffusion process of H^- and F^- inside T1 phase Sc_2C, Y_2C, and Zr_2C were studied computationally using NEB and compared against the diffusion process inside Ti_2C as covered in the previous sections. Subsequently, the obtained ground and transition states were analyzed using the Badelf code. The results are covered in Table 5 (for fluoride diffusion) and Table 6 (for hydride diffusion).

Structure	M		C		F		e^- charge	Diffusion barrier
	Ox. state	Volume (Å^3)	Ox. state	Volume (Å^3)	Ox. state	Volume (Å^3)		
Ti_2C	+2.50	5.28	-2.75	14.75	N/A	N/A	-0.64 (tetrahedral) -0.95 (octahedral)	0.26 eV
Ti_2CF_2 (T1)	+2.45	5.61	-3.23	17.24	-0.83	11.85	N/A	
$Ti_2CF_{1.97}$ (gs)	+2.46	5.62	-3.25	17.32	-0.84	12.23	-0.95	
$Ti_2CF_{1.97}$ (ts)	+2.46	5.60	-3.27	17.53	-0.84	12.75	-0.16	
Sc_2C (T1)	+2.22	6.86	-2.74	19.83	N/A	N/A	-0.86	0.09 eV
Sc_2CF_2 (T1)	+2.26	6.91	-2.81	21.23	-0.86	13.03	N/A	
$Sc_2CF_{1.97}$ (gs)	+2.26	6.95	-2.82	21.28	-0.88	14.07	N/A	
$Sc_2CF_{1.97}$ (ts)	+2.26	6.95	-2.83	21.29	-0.88	14.82	N/A	
Zr_2C (T1)	+2.81	7.84	-2.89	16.63	N/A	N/A	-0.73 (tetrahedral) -1.26 (octahedral)	0.05 eV
Zr_2CF_2 (T1)	+2.72	8.58	-3.73	21.88	-0.85	12.21	N/A	
$Zr_2CF_{1.96}$ (gs)	+2.73	8.58	-3.69	21.65	-0.86	12.33	-1.43	
$Zr_2CF_{1.96}$ (ts)	+2.72	8.61	-3.72	21.94	-0.86	13.07	-0.36	
Y_2C (T1)	+2.34	10.65	-2.99	24.07	N/A	N/A	-0.85	0.19 eV
Y_2CF_2 (T1)	+2.41	10.30	-3.07	26.90	-0.88	12.98	N/A	

$Y_2CF_{1.96}$ (gs)	+2.42	10.31	-2.91	25.87	-0.86	12.76	-1.08	
$Y_2CF_{1.96}$ (ts)	+2.41	10.36	-3.01	26.59	-0.89	15.70	N/A	

Table 5: Charge and volume analysis of atoms and electride sites in T1 phase M_2C during fluoride diffusion. For the ground state and transition state structures, the values reported for Ti and C are the global average, while the values for F^- are for the diffusing ion.

Structure	M		C		H		e^- charge	Diffusion barrier
	Ox. state	Volume (Å^3)	Ox. state	Volume (Å^3)	Ox. state	Volume (Å^3)		
Ti_2C	+2.50	5.28	-2.75	14.75	N/A	N/A	-0.64 (tetrahedral) -0.95 (octahedral)	0.71 eV
Ti_2CH_2 (T1)	+2.46	5.22	-2.95	16.61	-0.98	7.30	N/A	
$Ti_2CH_{1.97}$ (gs)	+2.48	5.15	-3.04	17.26	-0.96	7.01	-1.39	
$Ti_2CH_{1.97}$ (ts)	+2.49	5.15	-3.05	17.27	-1.97	15.7	N/A	
Sc_2C (T1)	+2.22	6.86	-2.74	19.83	N/A	N/A	-0.86	0.19 eV
Sc_2CH_2 (T1)	+2.23	6.73	-2.72	21.18	-0.87	9.77	N/A	
$Sc_2CH_{1.96}$ (gs)	+2.24	6.75	-2.75	21.34	-0.92	11.60	N/A	
$Sc_2CH_{1.96}$ (ts)	+2.24	6.75	-2.75	21.33	-0.93	12.93	N/A	
Zr_2C (T1)	+2.81	7.84	-2.89	16.63	N/A	N/A	-0.73 (tetrahedral) -1.26 (octahedral)	0.95 eV
Zr_2CH_2 (T1)	+2.78	7.75	-3.23	19.33	-0.99	7.71	N/A	
$Zr_2CH_{1.96}$ (gs)	+2.78	7.76	-3.17	18.94	-1.01	7.70	-1.5	
$Zr_2CH_{1.96}$ (ts)	+2.78	7.77	-3.19	19.00	-2.03	16.00	N/A	
Y_2C (T1)	+2.34	10.65	-2.99	24.07	N/A	N/A	-0.85	0.24 eV
Y_2CH_2 (T1)	+2.39	10.12	-2.95	26.03	-0.91	11.76	N/A	
$Y_2CH_{1.96}$ (gs)	+2.39	10.14	-2.89	25.63	-0.97	13.96	N/A	
$Y_2CH_{1.96}$ (ts)	+2.39	10.13	-2.89	25.65	-0.98	15.96	N/A	

Table 6: Charge and volume analysis of atoms and electride sites in T1 phase M_2C during hydride diffusion. For the ground state and transition state structures, the values reported for Ti and C are the global average, while the values for H^- are for the diffusing ion.

For fluoride diffusion inside M_2C materials, all of them have low diffusion barriers, and the order of increasing diffusion barrier is $Zr_2C < Sc_2C < Y_2C < Ti_2C$. Charge analysis of the moving fluoride atom reveals that for all structures save for Y_2C, the overall oxidation state and volume of fluoride changes very little during the diffusion process. Y_2C is a minor exception for this trend, as the volume of the diffusing F^- increases from 12.76 Å^3 to 15.7 Å^3 due to some 'elongation' similar to H^- in Ti_2C as described in the previous section (Figure 13a). However, the oxidation state of F^- still remains largely unchanged, and the 'elongation' does not seem to significantly negatively affect the diffusion barrier, as the obtained value was 0.19 eV, consistent with previous reports[20].

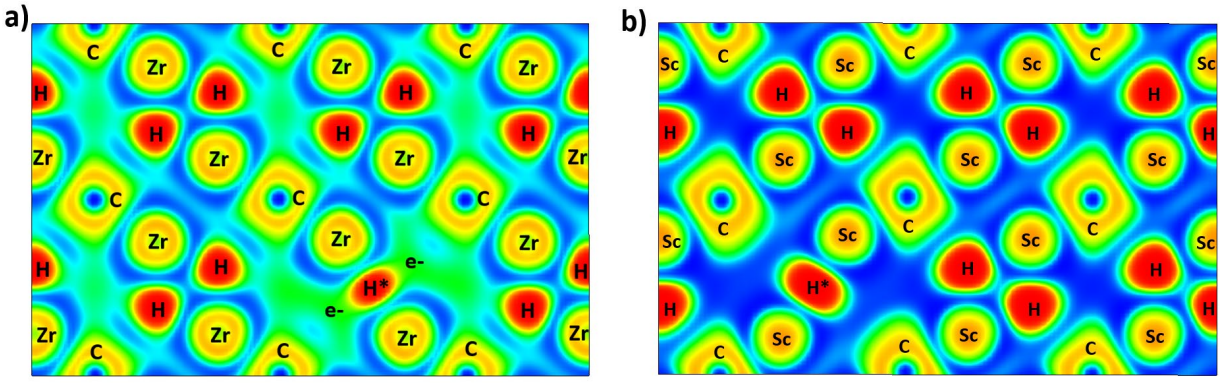


Figure 15: a) 2D ELF slice of the transition state of H^- diffusion inside Zr_2C, with atomic basins and electride basins labeled. The H atom denotes the moving hydride in its transition state, showing strong elongation and overlap towards the two electride sites. The ELF value at the two electride sites is 0.50. b) 2D ELF slice of the transition state of H^- diffusion inside Sc_2C, with atomic basins and electride basins labeled. The H* atom denotes the moving hydride in its transition state, showing elongation towards the two vacancy sites, but no interaction/overlap.*

On the other hand, hydride diffusion inside M_2C materials displays a stark difference between Group 3 metals and Group 4 metals. For Group 3 metals (Sc, Y), the diffusion barriers are small, only 0.19 eV for Sc_2C and 0.24 eV for Y_2C. For these structures, the H^- behaved similarly to F^- inside Y_2C (Figure 15), experiencing 'elongation' and volume expansion, but its oxidation state remains largely unchanged. However, M_2C materials containing Group 4 metals (Ti, Zr) were found to have rather high H^- diffusion barrier, with Ti_2C having a barrier of 0.71 eV as reported above, and Zr_2C having an even higher barrier at 0.95 eV. Similar to H^- in Ti_2C, charge analysis of H^- in Zr_2C reveals an anomalously high oxidation state of -2.02 and a volume of 16 $Å^3$ (over twice the typical H^- volume inside Zr_2C at 7 $Å^3$). A 2D slice of the electron localization function (ELF) of the transition state of the Zr_2C-H system (Fig 15a) displays the same behavior as Ti_2C: large elongation of the ELF shell and an interaction between H^- and the electride sites in the vacancies. This therefore further shows that interactions between H^- and the electride sites is likely the primary cause behind the very high diffusion barrier of H^- inside Zr_2C, instead of just the 'elongation' of the ion's shape. It's also interesting to notice that the hopping distance (and therefore the proximity of the ion in the transition state to the vacancy/electride sites) in Zr_2C and Sc_2C are very similar (the hopping distance is 2.29 Å in both materials), yet only the H^- in Zr_2C seems to interact with the electride sites (Fig 15), suggesting that distance alone is not enough to explain the different behavior of hydride. It's likely that other factors such as the contributions of the metal and carbon orbitals/states to the electride sites' character also play a role, though a further and deeper study of the materials' band structure and density of states will be used to verify this.

It had been suggested that the ionic radii overlap (ΔIRO), a quantifying descriptor of the sterics of the diffusing ion, can be used to predict the diffusion barrier of anions (particularly F^-) inside materials[48]. In particular, materials whose diffusion pathways involving the fluoride moving towards cations (positive ΔIRO_{cation}) and away from anions (negative ΔIRO_{anion}). Therefore, I computed the ΔIRO_{cation} and ΔIRO_{anion} values of the four M_2C materials to check whether they follow this trend. The calculated ΔIRO values are reported in Table 7 below.

Material	Diffusing ion	ΔIRO_{cation} (Å)	ΔIRO_{anion} (Å)	Diffusion barrier
Ti_2C	F^-	0.041	-0.0437	0.26 eV
Sc_2C	F^-	0.0715	-0.1297	0.09 eV
Zr_2C	F^-	0.0873	-0.102	0.05 eV
Y_2C	F^-	0.1435	-0.2226	0.19 eV
Ti_2C	H^-	0.1851	-0.2673	0.71 eV
Sc_2C	H^-	0.1332	-0.202	0.19 eV
Zr_2C	H^-	0.226	-0.3084	0.95 eV
Y_2C	H^-	0.1669	-0.2488	0.24 eV

Table 7: Calculated ΔIRO values for the diffusion of H^- and F^- inside considered materials

It can be seen that for all materials and for either H^- or F^-, the calculated ΔIRO_{cation} values are all positive and the ΔIRO_{anion} values are all negative. This fits with all the materials having diffusion barriers less than 1 eV. Looking at the specific trends among the materials, we see that for fluoride diffusion, Sc_2C, Ti_2C, and Zr_2C follow the expected trend that the larger magnitude of ΔIRO, the smaller the barrier, since the more the moving fluoride moves towards cations and away from anions, the more favorable the ionic radius overlaps will be. Y_2C once again remains a minor anomaly, as the magnitude of its ΔIRO values are quite higher than the rest, yet its diffusion barrier is the second highest among the four.

The problem becomes more interesting as the ΔIRO values for H^- diffusion are examined. It appears that the trend is opposite for H^- diffusion, as Zr_2C has the largest magnitude of ΔIRO but having the highest diffusion barrier. More interestingly, the magnitudes of ΔIRO of the hydride diffusions are similar to those of F^- diffusion in Y_2C, and in fact they together create a perfect trend that ΔIRO with larger magnitudes cause higher diffusion barriers. This aligns with the above assessments that H^- diffusion inside M_2C materials are more similar to F^- diffusion in Y_2C than in Sc_2C, Ti_2C, and Zr_2C. It can be explained that while the moving anion shifting away from other anions and closter to cations are initially thermodynamically favorable, shifting too close to the cation would cause internucleus repulsions, and in the case of H^- in Ti_2C and Zr_2C, inadvertently cause other unfavorable interactions with the host lattice.

However, these observed trends do not directly disprove the hypothesis that ΔIRO can be used to predict the diffusion barrier of anions. All the materials and diffusions considered have diffusion barriers under 1 eV, while the dataset considered by Sundberg et al. have materials with diffusion barriers up to 5 eV and ΔIRO values from -2 to 2 Å. This means that the differences between four considered M_2C materials will be very small compared to the large variety of materials considered by Sundberg et al., and ΔIRO alone is not enough to resolve.

IV. Computational methods

All DFT calculations used in this thesis were performed using the *meta*-GGA r^{2}SCAN functional[49] as implemented in the Vienna ab Initio Simulation Package (VASP)[50 51 52]. The project-augmented wave potentials[53] were used to describe core electrons and all calculations were performed taking spin polarization into account. For all the calculations (including those for the training of the machine-learned force fields unless stated otherwise in the following paragraphs), the plane-wave energy cutoff was 550 eV, the converge condition for electronic self-consistent loops was $1 * 10^{-6}\ eV$, and a gamma centered k-point grid with a spacing of 0.03 – 0.05 $2\pi/$Å was used, as generated by the vaspkit package[54] (the specific spacing value was chosen so that the condition $1000 \leq N_{kpts} * N_{atoms} \leq 2000$ is satisfied across all calculations). For most structural relaxations, except the NEB calculations as described below, the structures were relaxed in all degrees of freedom until the norms of all the forces were smaller than $0.02\ eV/$Å. Since most, if not all, structures involved in this study are metallic in nature, a 1st order Methfessel-Paxton smearing with a width of 30 meV was used across all calculations.

For the nudged elastic band (NEB) calculations, I created cubic supercells of the relaxed primitive unit cells of the fully hydrogenated or fluorinated $P\bar{3}m1$ T1 phase using pymatgen's CubicSupercellTransformation class[55]. The minimum lattice constants of the created cubic supercells were set to be 10 Å to ensure proper separation of periodic images. After the supercells were created, a single fluoride or hydride ion was removed to created the starting and ending structures, and then the obtained structures were relaxed using similar levels of theory as described above, except that only the atomic positions were relaxed. All NEB calculations were computed using 3 intermediate images, which were generated using the IDPP method as implemented in the pymatgen-analysis-diffusion add-on[56] for pymatgen.

Training structures for the cluster expansion models were generated using the structure enumeration function[57 58] as implemented in the ICET package. The cluster expansion models were trained using the automatic relevance detection regression (ARDR)[59] fitting method, and DFT input data was continually added to the model until the model successfully replicates the 0 K convex hull and the R^2 validation value exceeds 0.95. Monte Carlo simulations in the semi-grand canonical ensemble[35] were performed using the MCHAMMER module of the ICET[34 59] package, using supercells of 2000 – 5000 atoms. From the simulations, the chemical potential of fluoride or hydride were integrated using the trapezoid rule with respect to the fluoride / hydride concentration to obtain the free energy of the system.

Machine learned force fields (ML-FFs) were used in molecular dynamics for all structures. The ML-FFs were trained using the Flare package[37 38 39 40], which utilizes the sparse Gaussian process. For each structure, a supercell of 50 – 100 atoms were created with 1-2 fluorides or hydrides placed in each interlayer space. Compared to DFT calculations above, a less rigorous electronic convergence setting of $1 * 10^{-5}\ eV$ and a KSPACING value of 0.3 $Å^{-1}$ were used to save computational time. The maximum force uncertainty was set to 0.02 eV/Å. The Normalized Dot Product kernel was used with a sigma variance prefactor of 2.0 and power of 2. The local environment descriptor was the B2 descriptor of the atomic cluster expansion formalism, using a radial basis of 8 with 4 angular momentum harmonics. Chebyshev polynomials of the first kind were used with a simple quadratic cutoff with a distance of 5.0 Å. MD simulations of each phase were carried out using the LAMMPS[41 42] package using a NVT ensemble at a temperature range of 1100 – 1700 K (for T1 phase) and 1200 – 1700 K (for O3 phase), with 100 K intervals and a 1 fs (for F) or 0.1 fs (for H) timestep. The simulations were run for 11 days in real time, yielding a

simulation time between 2 - 4 ns (depending on the computing node used). Mean-squared displacement analysis of the obtained trajectories were carried out using the MDAnalysis package[60 61].

V. Conclusion

In this thesis, I have computationally investigated the properties of 2D layered electride Ti_2C as a fluoride-ion battery electride material and a hydrogen storage material. It had been shown that Ti_2C is a potential battery electrode material with decently low F^- diffusion barrier, high diffusion rate, suitable reduction potential, high theoretical capacities, but suffers from problems about lower favorability of F^- intercalation and large volume expansion upon fluorination. On the other hand, the intercalation of H^- into Ti_2C is more energetically favorable and causes insignificant volume expansion, but it has a higher H^- diffusion barrier and low diffusion coefficient.

More importantly, by comparing the behavior of F^- and H^- inside different materials with the formula M_2C and layered structure, I have shown that while H^- can resemble F^- in many aspects when intercalating and diffusing inside layered electrides, such as the ability to exchange for anionic electrons without causing redox reactions to the metal atoms, as well as causing insignificant changes to the host lattice during the diffusion step, there also exists stark differences between them, which primarily comes from the differences in size and polarizibility of the two ions. Furthermore, it is shown that the behavior of F^- and H^- inside M_2C electride materials vary at least somewhat systematically with the properties of the material's anionic electrons, which in turn correlates with the metal's group in the periodic table. This shows that it is worthwhile to study deeper and more carefully about the role of the metal ion in determining the properties of these electrides, and from that, devise design strategies for efficient anion conducting materials.

References

[1] Chen, Y.; Kang, Y.; Zhao, Y.; Wang, L.; Liu, J.; Li, Y.; Liang, Z.; He, X.; Li, X.; Tavajohi, N.; Li, B. A Review of Lithium-Ion Battery Safety Concerns: The Issues, Strategies, and Testing Standards. *Journal of Energy Chemistry* **2021**, *59*, 83–99. https://doi.org/10.1016/j.jechem.2020.10.017.

[2] Hwang, J.-Y.; Myung, S.-T.; Sun, Y.-K. Sodium-Ion Batteries: Present and Future. **2017**. https://doi.org/10.1039/C6CS00776G.

[3] Liang, Y.; Dong, H.; Aurbach, D.; Yao, Y. Current Status and Future Directions of Multivalent Metal-Ion Batteries. *Nat Energy* **2020**, *5* (9), 646–656. https://doi.org/10.1038/s41560-020-0655-0.

[4] Gopinadh, S. V.; Phanendra, P. V. R. L.; John, B.; Mercy, T. D. Fluoride-Ion Batteries: State-of-the-Art and Future Perspectives. *Sustainable Materials and Technologies* **2022**, *32*, e00436. https://doi.org/10.1016/j.susmat.2022.e00436.

[5] Gschwind, F.; Rodriguez-Garcia, G.; Sandbeck, D. J. S.; Gross, A.; Weil, M.; Fichtner, M.; Hörmann, N. Fluoride Ion Batteries: Theoretical Performance, Safety, Toxicity, and a Combinatorial Screening of New Electrodes. *Journal of Fluorine Chemistry* **2016**, *182*, 76–90. https://doi.org/10.1016/j.jfluchem.2015.12.002.

[6] Nowroozi, M. A.; Mohammad, I.; Molaiyan, P.; Wissel, K.; Munnangi, A. R.; Clemens, O. Fluoride Ion Batteries – Past, Present, and Future. *J. Mater. Chem. A* **2021**, *9* (10), 5980–6012. https://doi.org/10.1039/D0TA11656D.

[7] Liu, C.; Nikolaev, S. A.; Ren, W.; Burton, L. A. Electrides: A Review. *J. Mater. Chem. C* **2020**, *8* (31), 10551–10567. https://doi.org/10.1039/D0TC01165G.

[8] Hosono, H.; Kitano, M. Advances in Materials and Applications of Inorganic Electrides. *Chem. Rev.* **2021**, *121* (5), 3121–3185. https://doi.org/10.1021/acs.chemrev.0c01071.

[9] Zhang, X.; Yang, G. Recent Advances and Applications of Inorganic Electrides. *J. Phys. Chem. Lett.* **2020**, *11* (10), 3841–3852. https://doi.org/10.1021/acs.jpclett.0c00671.

[10] Kurashige, K.; Toda, Y.; Matstuishi, S.; Hayashi, K.; Hirano, M.; Hosono, H. Czochralski Growth of $12CaO{\cdot}7Al_2O_3$ Crystals. *Crystal Growth & Design* **2006**, *6* (7), 1602–1605. https://doi.org/10.1021/cg0600290.
[11] Weaver, S. M.; Lanetti, M. G.; Slamowitz, C. C.; Radomsky, R. C.; Warren, S. C. Assessing Dimensionality in Electrides. *J. Phys. Chem. C* **2025**, *129* (6), 3211–3217. https://doi.org/10.1021/acs.jpcc.4c06803.
[12] Sa, B.; Xiong, R.; Wen, C.; Li, Y.-L.; Lin, P.; Lin, Q.; Anpo, M.; Sun, Z. Electronic Anisotropy and Superconductivity in One-Dimensional Electride Ca_3Si. *J. Phys. Chem. C* **2020**, *124* (14), 7683–7690. https://doi.org/10.1021/acs.jpcc.0c00921.
[13] Chanhom, P.; Fritz, K. E.; Burton, L. A.; Kloppenburg, J.; Filinchuk, Y.; Senyshyn, A.; Wang, M.; Feng, Z.; Insin, N.; Suntivich, J.; Hautier, G. Sr_3CrN_3: A New Electride with a Partially Filled d-Shell Transition Metal. *J. Am. Chem. Soc.* **2019**, *141* (27), 10595–10598. https://doi.org/10.1021/jacs.9b03472.
[14] Zhang, X.; Xiao, Z.; Lei, H.; Toda, Y.; Matsuishi, S.; Kamiya, T.; Ueda, S.; Hosono, H. Two-Dimensional Transition-Metal Electride Y_2C. *Chem. Mater.* **2014**, *26* (22), 6638–6643. https://doi.org/10.1021/cm503512h.
[15] Lee, K.; Kim, S. W.; Toda, Y.; Matsuishi, S.; Hosono, H. Dicalcium Nitride as a Two-Dimensional Electride with an Anionic Electron Layer. *Nature* **2013**, *494* (7437), 336–340. https://doi.org/10.1038/nature11812.
[16] Mizoguchi, H.; Okunaka, M.; Kitano, M.; Matsuishi, S.; Yokoyama, T.; Hosono, H. Hydride-Based Electride Material, LnH_2 (Ln = La, Ce, or Y). *Inorg. Chem.* **2016**, *55* (17), 8833–8838. https://doi.org/10.1021/acs.inorgchem.6b01369.
[17] Meng, W.; Wang, J.; Wang, X.; Wang, W.; Zhang, X.; Bando, Y.; Cheng, Z. Multi-Dimensional Inorganic Electrides for Energy Conversion and Storage. *J. Mater. Chem. A* **2024**, *12* (5), 2583–2604. https://doi.org/10.1039/D3TA06546D.
[18] Hu, J.; Xu, B.; Yang, S. A.; Guan, S.; Ouyang, C.; Yao, Y. 2D Electrides as Promising Anode Materials for Na-Ion Batteries from First-Principles Study. *ACS Appl. Mater. Interfaces* **2015**, *7* (43), 24016–24022. https://doi.org/10.1021/acsami.5b06847.
[19] Hou, J.; Tu, K.; Chen, Z. Two-Dimensional Y_2C Electride: A Promising Anode Material for Na-Ion Batteries. *J. Phys. Chem. C* **2016**, *120* (33), 18473–18478. https://doi.org/10.1021/acs.jpcc.6b06087.
[20] Druffel, D. L.; Pawlik, J. T.; Sundberg, J. D.; McRae, L. M.; Lanetti, M. G.; Warren, S. C. First-Principles Prediction of Electrochemical Electron–Anion Exchange: Ion Insertion without Redox. *J. Phys. Chem. Lett.* **2020**, *11* (21), 9210–9214. https://doi.org/10.1021/acs.jpclett.0c02266.
[21] Hartman, S. T.; Mishra, R. Layered Electrides as Fluoride Intercalation Anodes. *J. Mater. Chem. A* **2020**, *8* (46), 24469–24476. https://doi.org/10.1039/D0TA06162J.
[22] Mondal, K.; Ghosh, P. Exfoliation of Ti_2C and Ti_3C_2 MXenes from Bulk Trigonal Phases of Titanium Carbide: A Theoretical Prediction. *Solid State Communications* **2019**, *299*, 113657. https://doi.org/10.1016/j.ssc.2019.113657.
[23] Wang, S.; Li, J.-X.; Du, Y.-L.; Cui, C. First-Principles Study on Structural, Electronic and Elastic Properties of Graphene-like Hexagonal Ti_2C Monolayer. *Computational Materials Science* **2014**, *83*, 290–293. https://doi.org/10.1016/j.commatsci.2013.11.025.
[24] Ahmad, H.; Mohd Makhfuz, M. J.; Yusoff, N.; Azam, A. D.; Samion, M. Z. Synthesis of 2D Titanium Carbide Ti_2C, Its Characteristics, and Nonlinear Optical Properties. *Optical Materials* **2023**, *135*, 113340. https://doi.org/10.1016/j.optmat.2022.113340.
[25] Liu, F.; Liu, Y.; Zhao, X.; Liu, K.; Yin, H.; Fan, L.-Z. Prelithiated V_2C MXene: A High-Performance Electrode for Hybrid Magnesium/Lithium-Ion Batteries by Ion Cointercalation. *Small* **2020**, *16* (8), 1906076. https://doi.org/10.1002/smll.201906076.
[26] Chen, Z.; Liu, Z.; Yuan, X.; Zhou, N. O- and S-Terminated M_2C MXenes as Anode Materials for Na/K-Ion Batteries. *J. Phys. Chem. C* **2022**, *126* (9), 4267–4275. https://doi.org/10.1021/acs.jpcc.1c09770.
[27] Shahpouri, E.; Kalantarian, M. M.; Ebadzadeh, T.; Mobasherpour, I. MXene M_2C (*M* = Ti, V, Cr, and Nb) as Electrode Material for Various Intercalation Batteries (Li, Na, Mg, Al, K, Ca, and Zn -Ion): *Ab-Initio* Studies. *Surfaces and Interfaces* **2026**, *80*, 108174. https://doi.org/10.1016/j.surfin.2025.108174.
[28] Naguib, M.; Come, J.; Dyatkin, B.; Presser, V.; Taberna, P.-L.; Simon, P.; Barsoum, M. W.; Gogotsi, Y. MXene: A Promising Transition Metal Carbide Anode for Lithium-Ion Batteries. *Electrochemistry Communications* **2012**, *16* (1), 61–64. https://doi.org/10.1016/j.elecom.2012.01.002.
[29] Renaudin, G.; Yvon, K.; Dolukhanyan, S. K.; Aghajanyan, N. N.; Shekhtman, V. Sh. Crystal Structures and Thermal Properties of Titanium Carbo-Deuterides as Prepared by Combustion Synthesis. *Journal of Alloys and Compounds* **2003**, *356–357*, 120–127. https://doi.org/10.1016/S0925-8388(03)00107-5.

[30] Yang, X.-Y.; Luo, W.; Ahuja, R. Fluoride Ion Batteries: Designing Flexible M_2CH_2 (M=Ti or V) MXenes as High-Capacity Cathode Materials. *Nano Energy* **2020**, *74*, 104911. https://doi.org/10.1016/j.nanoen.2020.104911.
[31] Wang, S.; Du, Y.; Liao, W.; Sun, Z. Hydrogen Adsorption, Dissociation and Diffusion on Two-Dimensional Ti_2C Monolayer. *International Journal of Hydrogen Energy* **2017**, *42* (44), 27214–27219. https://doi.org/10.1016/j.ijhydene.2017.09.111.
[32] An Introduction to Density Functional Theory in Chemistry. In *Theoretical and Computational Chemistry*; Elsevier, 1995; Vol. 2, pp 1–27. https://doi.org/10.1016/S1380-7323(05)80031-7.
[33] Wu, Q.; He, B.; Song, T.; Gao, J.; Shi, S. Cluster Expansion Method and Its Application in Computational Materials Science. *Computational Materials Science* **2016**, *125*, 243–254. https://doi.org/10.1016/j.commatsci.2016.08.034.
[34] Ångqvist, M.; Muñoz, W. A.; Rahm, J. M.; Fransson, E.; Durniak, C.; Rozyczko, P.; Rod, T. H.; Erhart, P. ICET – A Python Library for Constructing and Sampling Alloy Cluster Expansions. *Advanced Theory and Simulations* **2019**, *2* (7), 1900015. https://doi.org/10.1002/adts.201900015.
[35] Marquez, F. M.; Cienfuegos, C.; Pongsai, B. K.; Lavrentiev, M. Y.; Allan, N. L.; Purton, J. A.; Barrera, G. D. Semigrand-Canonical Ensemble Simulations of the Phase Diagrams of Alloys. *Modelling Simul. Mater. Sci. Eng.* **2003**, *11* (2), 115. https://doi.org/10.1088/0965-0393/11/2/301.
[36] Lithium-Ion Batteries. **2022**, 5–13. https://doi.org/10.1016/B978-0-12-819723-3.00102-5.
[37] Xie, Y.; Vandermause, J.; Ramakers, S.; Protik, N. H.; Johansson, A.; Kozinsky, B. Uncertainty-Aware Molecular Dynamics from Bayesian Active Learning for Phase Transformations and Thermal Transport in SiC. *npj Comput Mater* **2023**, *9* (1), 36. https://doi.org/10.1038/s41524-023-00988-8.
[38] Vandermause, J.; Xie, Y.; Lim, J. S.; Owen, C. J.; Kozinsky, B. Active Learning of Reactive Bayesian Force Fields Applied to Heterogeneous Catalysis Dynamics of H/Pt. *Nat Commun* **2022**, *13* (1), 5183. https://doi.org/10.1038/s41467-022-32294-0.
[39] Vandermause, J.; Torrisi, S. B.; Batzner, S.; Xie, Y.; Sun, L.; Kolpak, A. M.; Kozinsky, B. On-the-Fly Active Learning of Interpretable Bayesian Force Fields for Atomistic Rare Events. *npj Comput Mater* **2020**, *6* (1), 20. https://doi.org/10.1038/s41524-020-0283-z.
[40] Xie, Y.; Vandermause, J.; Sun, L.; Cepellotti, A.; Kozinsky, B. Bayesian Force Fields from Active Learning for Simulation of Inter-Dimensional Transformation of Stanene. *npj Comput Mater* **2021**, *7* (1), 40. https://doi.org/10.1038/s41524-021-00510-y.
[41] Thompson, A. P.; Aktulga, H. M.; Berger, R.; Bolintineanu, D. S.; Brown, W. M.; Crozier, P. S.; in 't Veld, P. J.; Kohlmeyer, A.; Moore, S. G.; Nguyen, T. D.; Shan, R.; Stevens, M. J.; Tranchida, J.; Trott, C.; Plimpton, S. J. LAMMPS - a Flexible Simulation Tool for Particle-Based Materials Modeling at the Atomic, Meso, and Continuum Scales. *Computer Physics Communications* **2022**, *271*, 108171. https://doi.org/10.1016/j.cpc.2021.108171.
[42] Gissinger, J. R.; Nikiforov, I.; Afshar, Y.; Waters, B.; Choi, M.; Karls, D. S.; Stukowski, A.; Im, W.; Heinz, H.; Kohlmeyer, A.; Tadmor, E. B. Type Label Framework for Bonded Force Fields in LAMMPS. *J. Phys. Chem. B* **2024**, *128* (13), 3282–3297. https://doi.org/10.1021/acs.jpcb.3c08419.
[43] Weaver, S. M.; Sundberg, J. D.; Slamowitz, C. C.; Radomsky, R. C.; Lanetti, M. G.; McRae, L. M.; Warren, S. C. Counting Electrons in Electrides. *J. Am. Chem. Soc.* **2023**, *145* (48), 26472–26476. https://doi.org/10.1021/jacs.3c10876.
[44] Xu, W.; Sun, L.; Zhai, W.; Yang, J.; Jiang, T.; Peng, J. Exploring Hydrogen Adsorption and Release in 2D M_2C-MXenes: Structural and Functional Insights. *Nanotechnology* **2024**, *36* (9), 095702. https://doi.org/10.1088/1361-6528/ad9bb8.
[45] Onoda, M.; Shi, Y.; Leithe-Jasper, A.; Tanaka, T. Structure Refinement of the Layered Composite Crystal $Sc_2B_{1.1}C_{3.2}$ in a Five-Dimensional Formalism. *Acta Crystallogr B* **2001**, *57* (Pt 4), 449–457. https://doi.org/10.1107/s0108768101006607.
[46] Thomas, S. A.; Cherusseri, J. Recent Advances in Synthesis and Properties of Zirconium-Based MXenes for Application in Rechargeable Batteries. *Energy Storage* **2023**, *5* (8), e475. https://doi.org/10.1002/est2.475.
[47] Kang, S. H.; Bang, J.; Chung, K.; Nandadasa, C. N.; Han, G.; Lee, S.; Lee, K. H.; Lee, K.; Ma, Y.; Oh, S. H.; Kim, S.-G.; Kim, Y.-M.; Kim, S. W. Water- and Acid-Stable Self-Passivated Dihafnium Sulfide Electride and Its Persistent Electrocatalytic Reaction. *Science Advances* **2020**, *6* (23), eaba7416. https://doi.org/10.1126/sciadv.aba7416.

[48] Sundberg, J. D.; Druffel, D. L.; McRae, L. M.; Lanetti, M. G.; Pawlik, J. T.; Warren, S. C. High-Throughput Discovery of Fluoride-Ion Conductors via a Decoupled, Dynamic, and Iterative (DDI) Framework. *npj Comput Mater* **2022**, *8* (1), 106. https://doi.org/10.1038/s41524-022-00786-8.
[49] Furness, J. W.; Kaplan, A. D.; Ning, J.; Perdew, J. P.; Sun, J. Accurate and Numerically Efficient r2SCAN Meta-Generalized Gradient Approximation. *J. Phys. Chem. Lett.* **2020**, *11* (19), 8208–8215. https://doi.org/10.1021/acs.jpclett.0c02405.
[50] Kresse, G.; Furthmüller, J. Efficient Iterative Schemes for Ab Initio Total-Energy Calculations Using a Plane-Wave Basis Set. *Phys. Rev. B* **1996**, *54* (16), 11169–11186. https://doi.org/10.1103/PhysRevB.54.11169.
[51] Kresse, G.; Furthmüller, J. Efficiency of Ab-Initio Total Energy Calculations for Metals and Semiconductors Using a Plane-Wave Basis Set. *Computational Materials Science* **1996**, *6* (1), 15–50. https://doi.org/10.1016/0927-0256(96)00008-0.
[52] Kresse, G.; Hafner, J. Ab Initio Molecular Dynamics for Liquid Metals. *Phys. Rev. B* **1993**, *47* (1), 558–561. https://doi.org/10.1103/PhysRevB.47.558.
[53] Kresse, G.; Joubert, D. From Ultrasoft Pseudopotentials to the Projector Augmented-Wave Method. *Phys. Rev. B* **1999**, *59* (3), 1758–1775. https://doi.org/10.1103/PhysRevB.59.1758.
[54] Wang, V.; Xu, N.; Liu, J.-C.; Tang, G.; Geng, W.-T. VASPKIT: A User-Friendly Interface Facilitating High-Throughput Computing and Analysis Using VASP Code. *Computer Physics Communications* **2021**, *267*, 108033. https://doi.org/10.1016/j.cpc.2021.108033.
[55] Ong, S. P.; Richards, W. D.; Jain, A.; Hautier, G.; Kocher, M.; Cholia, S.; Gunter, D.; Chevrier, V. L.; Persson, K. A.; Ceder, G. Python Materials Genomics (Pymatgen): A Robust, Open-Source Python Library for Materials Analysis. *Computational Materials Science* **2013**, *68*, 314–319. https://doi.org/10.1016/j.commatsci.2012.10.028.
[56] Deng, Z.; Zhu, Z.; Chu, I.-H.; Ong, S. P. Data-Driven First-Principles Methods for the Study and Design of Alkali Superionic Conductors. *Chem. Mater.* **2017**, *29* (1), 281–288. https://doi.org/10.1021/acs.chemmater.6b02648.
[57] Hart, G. L. W.; Forcade, R. W. Algorithm for Generating Derivative Structures. *Phys. Rev. B* **2008**, *77* (22), 224115. https://doi.org/10.1103/PhysRevB.77.224115.
[58] Hart, G. L. W.; Forcade, R. W. Generating Derivative Structures from Multilattices: Algorithm and Application to Hcp Alloys. *Phys. Rev. B* **2009**, *80* (1), 014120. https://doi.org/10.1103/PhysRevB.80.014120.
[59] Ekborg-Tanner, P.; Rosander, P.; Fransson, E.; Erhart, P. Construction and Sampling of Alloy Cluster Expansions---A Tutorial. *PRX Energy* **2024**, *3* (4), 042001. https://doi.org/10.1103/PRXEnergy.3.042001.
[60] Gowers, R. J.; Linke, M.; Barnoud, J.; Reddy, T. J. E.; Melo, M. N.; Seyler, S. L.; Domański, J.; Dotson, D. L.; Buchoux, S.; Kenney, I. M.; Beckstein, O. MDAnalysis: A Python Package for the Rapid Analysis of Molecular Dynamics Simulations. *SciPy 2016* **2016**. https://doi.org/10.25080/Majora-629e541a-00e.
[61] Michaud-Agrawal, N.; Denning, E. J.; Woolf, T. B.; Beckstein, O. MDAnalysis: A Toolkit for the Analysis of Molecular Dynamics Simulations. *Journal of Computational Chemistry* **2011**, *32* (10), 2319–2327. https://doi.org/10.1002/jcc.21787.